Astronomy & Astrophysics manuscript no. ms
February 19, 2019

TESS first look at evolved compact pulsators

Discovery and asteroseismic probing of the *g*-mode hot B subdwarf pulsator TIC 278659026

S. Charpinet[1], P. Brassard[2], G. Fontaine[2], V. Van Grootel[3], W. Zong[4], N. Giammichele[1], U. Heber[5], Zs. Bognár[6,7], S. Geier[8], E.M. Green[9], J.J. Hermes[10], D. Kilkenny[11], R.H. Østensen[12], I. Pelisoli[8], R. Silvotti[13], J.H. Telting[14], M. Vučković[15], H.L. Worters[16], A.S. Baran[17], K.J. Bell[18], P.A. Bradley[19], J.H. Debes[20], S.D. Kawaler[21], P. Kołaczek-Szymański[22], S.J. Murphy[23], A. Pigulski[22], À. Sódor[6,7], and M. Uzundag[15]

(Affiliations can be found after the references)

Received ...; Accepted...

ABSTRACT

Context. The *TESS* satellite was recently launched to perform high-precision photometry from space over almost the whole sky in a search for exoplanets smaller than Neptune. It is also opening new opportunities to study all kind of variabilities encountered in hot subdwarfs, white dwarfs, and related compact objects. Targets of interest include, in particular, white-dwarf and hot-subdwarf pulsators, both carrying high potential for asteroseismology.

Aims. We present the discovery and detailed asteroseismic analysis of a new *g*-mode hot B subdwarf (sdB) pulsator, TIC 278659026 (EC 21494-7018), monitored in *TESS* first sector using 120-second cadence.

Methods. The *TESS* light curve is analysed using standard prewhitening techniques. We then apply a forward modelling optimization using our latest generation of sdB models developed for asteroseismic investigations. By best-matching simultaneously all the frequencies identified in TIC 278659026 and attributed to independent *g*-modes with those computed from models, we identify the pulsation modes detected and, more importantly, we determine the global parameters and structural configuration of the star.

Results. The light curve analysis reveals that TIC 278659026 is a long-period sdB pulsator with a rich frequency spectrum. Among the detected signals, 20 frequencies found in the $96-605$ μHz range are associated with independent *g*-modes. Weak peaks are also present at very low frequency. The seismic analysis singles out one optimal model solution that can best account for the observed pulsation properties of TIC 278659026. This solution is in full agreement with independent measurements provided by spectroscopy (atmospheric parameters derived from model atmospheres) and astrometry (distance evaluated from *Gaia* DR2 trigonometric parallax). Several key parameters of the star are derived. Its mass (0.391 ± 0.013 $M_\odot$; significantly lower than the typical mass of sdB stars) suggests that its progenitor has not undergone He-flash, and therefore could originate from a massive ($\gtrsim 2$ $M_\odot$) red giant, an alternative channel for the formation of hot B subdwarfs. Other derived parameters include the H-rich envelope mass (0.0037 ± 0.0017 $M_\odot$), radius (0.1694 ± 0.0081 $R_\odot$), and luminosity (8.2 ± 1.1 $L_\odot$). Moreover, a relatively clear view of the internal chemical stratification inside TIC 278659026 has emerged from this seismic probing. The H-rich envelope structure providing an optimal fit to the observed frequencies features a double-layered He/H composition profile, interpreted as the still ongoing gravitational settling of helium at the bottom of a rather thick envelope. We also derive the properties of the core, indicating that TIC 278659026 has burnt $\sim 43\%$ (in mass) of its central helium and possesses a relatively large mixed core ($M_{\rm core} = 0.198 \pm 0.015$ $M_\odot$). This latter measurement is in line with trends already uncovered for other g-mode sdB pulsators analysed with asteroseismology. Finally, we obtain for the first time an estimate of the amount of oxygen (in mass; $X(\mathrm{O})_{\rm core} = 0.16^{+0.13}_{-0.07}$) produced at this stage of evolution by an helium-burning core. This result, along with the core-size estimate, could provide interesting constraints for future studies concerning the still uncertain $^{12}\mathrm{C}(\alpha,\gamma)^{16}\mathrm{O}$ nuclear reaction rate.

Conclusions. This seismic analysis of TIC 278659026 is a clear demonstration that *TESS*, despite being optimized for planet detection, delivers exceptional data for asteroseismology of hot B subdwarf stars. One can anticipate that its impact on the field, considering the large number of stars ultimately monitored, will be enormous.

Key words. stars: oscillations – stars: interiors – stars: horizontal-branch – subdwarfs – stars: individual: TIC 278659026

1. Introduction

The NASA *Transiting Exoplanet Survey Satellite* (*TESS*), successfully launched on 2018 April 18, is the latest instrument dedicated to high-precision photometric monitoring of stars from space. Besides its main objective to identify new exoplanets transiting nearby stars (Ricker et al. 2014), *TESS* is expected to contribute significantly to the study of stellar variability, extending in particular the use of asteroseismology for all types of pulsating stars. An important asset of *TESS*, compared to its predecessors – *K2* (Howell et al. 2014), *Kepler* (Borucki et al. 2010; Gilliland et al. 2010), *CoRoT* (Baglin et al. 2006), and *MOST* (Walker et al. 2003) – is the much more extended sky coverage as, during the two-year duration of the main mission, the satellite will survey over 90% of the sky, avoiding only a narrow band around the ecliptic already explored, in part, by *K2*.

The *TESS* nominal two-year survey is sectorized, with each sector consisting of a nearly continuous observation

Send offprint requests to: S. Charpinet

of the same field for about 27 days. Some overlap between sectors exists for the highest northern and southern ecliptic latitudes, meaning that some stars can be observed longer. In particular, stars located in the Continuous Viewing Zone (CVZ), close to the ecliptic caps, could benefit from as much as about one year of monitoring. *TESS* data products include Full-Frame Images (FFI) taken every 30 minutes and containing the entire field of view, as well as short-cadence observations sampled every 120 seconds, providing a better time resolution for a selection of approximately 16,000 stars per sector. An even faster 20 s-cadence mode is also considered for a small selection of fast varying objects, but this "ultra short" sampling rate is not yet available.

Important efforts have been carried out since 2015 to assemble specific lists of evolved compact stars, mostly white dwarfs and hot subdwarfs, to be submitted for the shortest cadence modes. This was coordinated through the *TESS Asteroseismic Science Consortium* (TASC)[1] Working Group 8 (WG8), which ultimately proposed an extensive variability survey using the *TESS* 120 s-cadence mode for all known evolved compact stars brighter than $\sim 16^{\rm th}$ magnitude. A shorter list of selected objects, mostly fast white-dwarf and hot-subdwarf pulsators that critically depend on the planned 20 s-sampling, was also constructed and is kept updated in case this observation mode becomes available. These target lists were assembled from existing catalogs of hot-subdwarf and white-dwarf stars, further enriched by discoveries of new objects of this kind obtained by dedicated efforts conducted from ground-based facilities[2]. To date, approximately 1,800 white dwarfs and 3,100 hot subdwarf stars are scheduled to be observed by *TESS* as part of the TASC WG8 120s-cadence list, while the 20s-cadence list counts approximately 400 targets[3]. These lists are constantly updated as efforts to identify new white dwarfs and hot subdwarfs continue, especially in light of *Gaia* DR2.

Monitoring pulsating hot B subdwarf (sdB) stars with *TESS* is one among several objectives pursued by TASC WG8. The occurrence of nonradial pulsations in sdB stars provides an extraordinary way, through asteroseismology, to probe their inner structure and dynamics. Hot B subdwarfs are associated with the so-called Extreme Horizontal Branch (EHB), forming a blue extension to the Horizontal Branch. These stars correspond to low-mass (typically $\sim 0.47\ M_\odot$) objects burning helium in their cores (see Heber 2016, for a recent review on the subject), and as such, they are representative of this intermediate phase of stellar evolution. They differ from classical Horizontal Branch stars mainly at the level of their residual H-rich envelope, which has been strongly reduced during the previous stage of evolution, leaving only a thin layer less massive than $\sim 0.02\ M_\odot$. As a consequence, sdB stars remain hot and compact ($T_{\rm eff} \sim 22\,000$ – $40\,000$ K, log g ~ 5.2 – 6.2; Saffer et al. 1994) throughout their He-burning lifetime (~ 150 Myr), and never ascend the Asymptotic Giant Branch before reaching the white dwarf cooling tracks (e.g., Dorman et al. 1993).

Two main classes of sdB pulsators have offered, so far, the opportunity to use asteroseismology to investigate this intermediate evolutionary stage. The *V361 Hya* stars (also named sdBV$_{\rm r}$ or *EC14026* stars from the class prototype; Kilkenny et al. 1997 and see the nomenclature proposed by Kilkenny et al. 2010) were the first to be discovered and oscillate rapidly with periods typically in the 80 – 600 s range that correspond to low-order, low-degree p-modes. These modes are driven by a classical κ-mechanism produced by the accumulation of iron-group elements in the "Z-bump" region (Charpinet et al. 1996). This accumulation is triggered by radiative levitation (Charpinet et al. 1997, 2001). The second group is the *V1093 Her* stars (sdBV$_{\rm s}$, PG1716, or "Betsy" stars; Green et al. 2003) that pulsate far more slowly with periods typically in the $1 - 4$ hour range, corresponding to mid-order gravity (g-)modes driven by the same mechanism (Fontaine et al. 2003; Jeffery & Saio 2006). A fraction of these stars belongs to both classes and are usually referred to as hybrid pulsators (also known as the *DW Lyn* or sdBV$_{rs}$ stars; Schuh et al. 2006).

The advent of space-borne, high-photometric-accuracy instruments has played a fundamental role in unlocking the application of asteroseismology to the long-period $g-$mode sdB pulsators. Prior to this "space age", detailed asteroseismology of sdB stars was limited to *V361 Hya* pulsators (e.g., Charpinet et al. 2008, and references therein). Despite important efforts carried out from the ground (Randall et al. 2006a,b; Baran et al. 2009), it had proved extremely difficult to differentiate g-mode pulsation frequencies from aliases introduced by the lack of continuous coverage, particularly due to the long periods and low amplitudes ($\sim 0.1\%$) typically involved. This difficulty was overcome when *CoRoT* and *Kepler* observations (Charpinet et al. 2010; Østensen et al. 2010, 2011) first provided much clearer views of the g-mode spectrum in these stars. Since then, many studies based mostly on *Kepler* and *K2* data have enriched our general understanding of g-mode pulsations in hot B subdwarfs, and in some case provided new insight on various properties of these stars (e.g., Reed et al. 2011; Østensen et al. 2014; Telting et al. 2014; Zong et al. 2016a; Baran et al. 2017; Kern et al. 2017; Ketzer et al. 2017; Zong et al. 2018; Reed et al. 2019), such as their rotation rate (see, e.g., Reed et al. 2014; Charpinet et al. 2018, and references therein).

However, to date, detailed *quantitative* asteroseismic inferences of the internal structure of sdB stars exist only for a dozen p-mode pulsators (see, e.g., Van Grootel et al. 2008a,b; Charpinet et al. 2008; Randall et al. 2009; Fontaine et al. 2012, and references therein) and three g-mode pulsators (Van Grootel et al. 2010a,b; Charpinet et al. 2011). The latter analyses have established the great potential of g-mode asteroseismology that was envisioned for these stars. Gravity modes, because they propagate far into the stellar interior, as opposed to p-modes, which remain confined to the outermost layers (Charpinet et al. 2000), have the potential to reveal the structure of the deepest regions, including the thermonuclear furnace and the core boundary structure (Charpinet et al. 2014b,a; Ghasemi et al. 2017). Van Grootel et al. (2010a,b) and Charpinet et al. (2011) showed that important constraints on the inner core, such as its chemical composition (related to the age of the star on the EHB) and its size, are indeed accessible, suggest-

[1] `https://tasoc.dk`

[2] Dedicated efforts in preparation of *TESS* have been carried out from Steward Observatory (U. of Arizona, USA), Nordic Optical Telescope (Spain), South African Astronomical Observatories (South Africa), Piszkéstető (Konkoly Observatory, Hungary).

[3] Information can be found from TASC WG8 wiki pages at `https://tasoc.dk/wg8`

ing in particular that the mixed core may be larger than expected. This would imply that efficient extra mixing processes (e.g., core convection overshoot, semi-convection) are effective. More analyses of this kind, with improved modelling tools, are required to fully and objectively map the internal properties of hot subdwarf stars. The *Kepler* and *K2* legacy is already providing a remarkable set of seismic data that remains to be fully exploited in that context, but *TESS* adds another dimension at this level, with the promise of expanding considerably the sample of objects exploitable through asteroseismology.

As anticipated, the delivery of the *TESS* data for hundreds of selected TASC WG8 targets monitored in the first four sectors has revealed a wealth of photometric variations occuring in all types of evolved compact stars, including many eclipsing or non-eclipsing binaries and compact pulsators. These will be presented in forthcoming dedicated publications. Here, we focus on one of these objects, TIC 278659026 (EC 21494-7018), whose observation establishes that it is a bright, long-period pulsating sdB star that was not previously known to pulsate. The data reveal a particularly clean and rich pulsation spectrum, making this star a perfect target to attempt a detailed asteroseismic study. We present in Sect. 2, the analysis of the *TESS* light curve obtained for TIC 278659026, which constitutes the basis of the detailed asteroseismic study that follows in Sect. 3. We summarize our results and conclusions in Sect. 4.

2. Observations

2.1. About TIC 278659026

TIC 278659026 (also known as EC 21494-7018; O'Donoghue et al. 2013)[4] is a bright, $V = 11.57 \pm 0.09$ (Høg et al. 2000) or $G = 11.5928 \pm 0.0009$ (Gaia Collaboration et al. 2016, 2018), blue high-proper-motion object first identified as a potential hot subdwarf by Jiménez-Esteban et al. (2011). Its classification was later confirmed by Németh et al. (2012) on the basis of a detailed spectroscopic analysis of its atmosphere using non-LTE models that gives $T_{\rm eff} = 23720 \pm 260$ K, $\log g = 5.65 \pm 0.03$, and $\log({\rm He/H}) = -3.22^{+0.13}_{-1.13}$ for this star. The rather high surface gravity and low effective temperature imply a position for TIC 278659026 below the standard, $M = 0.47\ M_\odot$, Zero Age Extreme Horizontal Branch, indicating that it might be less massive than typical hot B subdwarf stars. Kawka et al. (2015) indeed suggested that it could be a rare Extremely Low-Mass (ELM) white-dwarf progenitor, although they did not detect any significant radial velocity variations indicating the presence of a companion. Their average radial velocity measurement and dispersion is 43.4 ± 4.2 km.s^{-1}, which is consistent with the independent measurement of 39.4 ± 7.5 km.s^{-1} from Copperwheat et al. (2011), who did not find any variability either. The photometry available for this star (see Sect. 3.4.1) rule out any main sequence companion that would be earlier than type M5/M6.

Geier & Heber (2012) reported a projected rotational velocity of $v_{\rm rot} \sin i = 8.6 \pm 1.8$ km.s^{-1} for EC 21494-7018, which is close to the average value measured in their sample of 105 sdB stars. These estimates are obtained by modeling the broadening of metal lines in high-resolution optical spectra, as described in Geier et al. (2010). A critical look at the FEROS spectrum of EC 21494-7018 reveals, however, that its S/N is not excellent, and only three metal lines could be used to estimate the projected rotational velocity, due to the low temperature of the star. Therefore, caution is advised concerning this particular measurement (see also the discussion of Sect. 3.1).

[4] Other names for this star are TYC 9327-1311-1, GSC 09327-01311, 2MASS J21534125-7004314, GALEX J215341.2-700431, and *Gaia* DR2 6395639996658760832.

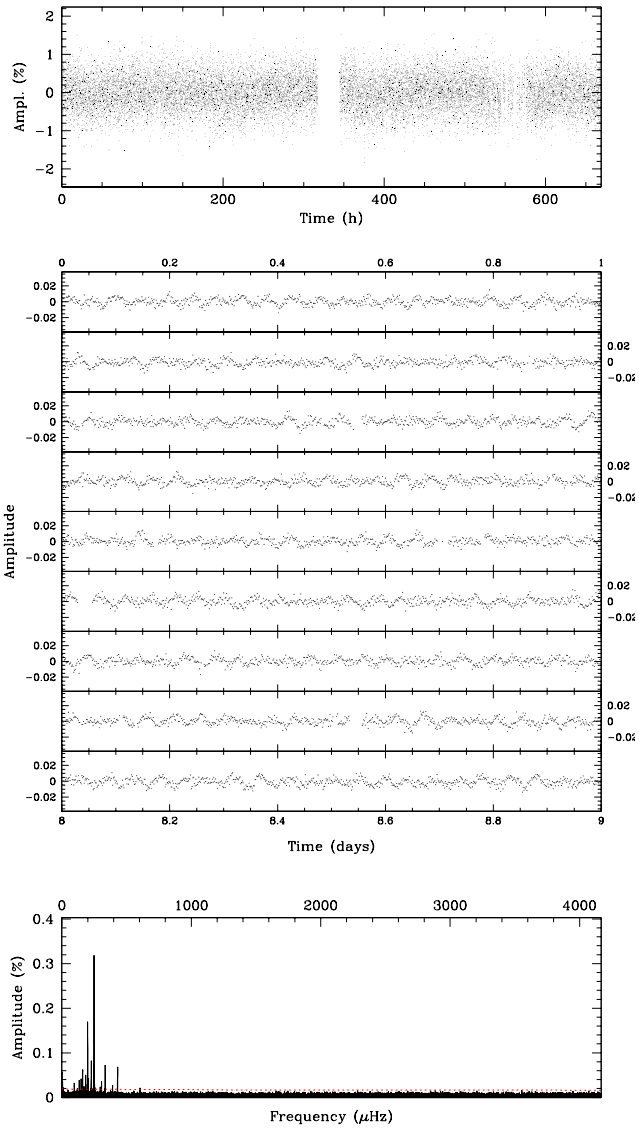

Fig. 1. Illustration of *TESS* photometry obtained for TIC 278659026. *Top panel* shows the entire light curve (amplitude is in percent of the mean brightness of the star) spanning 27.88 days sampled every 120 seconds. Holes in this time series are due to the mid-sector interruption during data download and missing points removed from the light curve because of a non-optimal quality flag warning. *Middle panel* shows an expanded view of the light curve covering the first 9 days, where modulations due to pulsations are clearly visible (note that amplitude is given as the fraction of the mean brightness here). *Bottom panel* shows the Lomb-Scargle Periodogram (LSP) of the light curve up to the Nyquist frequency limit corresponding to the sampling rate (~ 4467 μHz). The horizontal dotted line indicates 4 times the median noise level. Significant activity well above this threshold and in a frequency range corresponding to g-mode pulsations is clearly detected.

2.2. TESS Photometry

TIC 278659026 was observed in *TESS* Sector 1, from July 25 to August 22, 2018. As a rather bright hot B subdwarf star, it was positioned at a relatively high priority rank among the stars proposed by the TASC Working Group 8, despite having no previously known variability due to pulsations or other causes, because its atmospheric parameters, $T_{\rm eff}$ and $\log g$, places it well within the hot B subdwarf g-mode instability region (see, e.g., Figure 4 of Charpinet et al. 2009). The TIC 278659026 time series consists of 18102 individual photometric measurements[5] obtained with the 120s-cadence mode, covering almost continuously 27.88 days (669.12 hours) of observation. We base our analysis on the corrected time series extracted with the *TESS* data processing pipeline developed by the Science Processing Operations Center (SPOC) at NASA Ames Research Center. These light curves are delivered publicly along with pixel data at the *Mikulski* Archive for Space Telescope (MAST).

The top panel of Fig. 1 illustrates the TIC 278659026 light curve in its entirety. The apparent amplitude scatter visible at this scale shows up as a clearly multiperiodic signal in the close-up view focusing on 9 days of observation presented in the middle panel of Fig. 1. A Lomb-Scargle Periodogram of the time series[6] (LSP; bottom panel of Fig. 1) confirms the presence of highly coherent low-amplitude modulations of the star brightness, with timescales ranging from 27 minutes to 2.89 hours. Such variations are typical of $g-$mode oscillations in hot subdwarf stars. Additional weak signals are also possibly present at the very low frequency range (< 5 μHz), but could be of instrumental origin. In contrast, no significant peaks are found in the LSP at higher frequencies, up to the Nyquist limit. Hence, these *TESS* data clearly establish that TIC 278659026 is a new bright pulsating sdB star of the *V1093 Her* class.

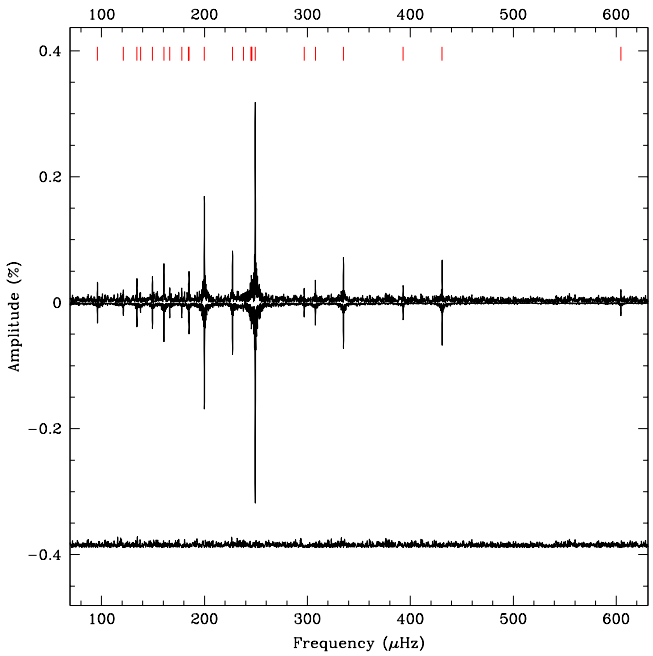

Fig. 2. Frequencies detected in the g-mode pulsation range. The upper curve shows a close-up view of the Lomb-Scargle Periodogram (LSP) computed from TIC 278659026 light curve. Each small vertical segment indicates a frequency extracted during the prewhitening and nonlinear least-square fitting analysis. All frequencies and their properties are tabulated in Table 1. The curve plotted upside-down is a reconstruction of the LSP based on the data summarized in this table, and the curve at the bottom (shifted vertically by an arbitrary amount for visibility) is the residual containing only noise after removing all the signal from the light curve. No peak above 4 times the average noise level is left in this residual.

2.3. The g-mode pulsation spectrum

We performed a standard prewhitening and nonlinear least-square fitting analysis to extract the frequencies present in the brightness modulations of TIC 278659026 (Deeming 1976). For that purpose, we used the dedicated software FELIX (Charpinet et al. 2010, see also Zong et al. 2016a), which greatly facilitates the application of this procedure. Most of the coherent variability is found to reside in the 95 – 650 μHz range where we could easily extract up to 23 frequencies above a chosen detection threshold at 4 times the median noise level[7] (see Table 1). The result of this extraction is illustrated in Fig. 2, showing that the signal in Fourier space reconstructed from the 23 identified frequencies (plotted upside-down) reproduces very well the periodogram of the *TESS* light curve and no significant residual is found after substraction of this signal. Close-up views of the most relevant parts of the spectrum are also provided in Fig. 3. In effect, the lowest amplitude peak extracted has a S/N ratio of 4.4, well above the 4σ threshold. In order to estimate how reliable are the lowest amplitude peaks of our selection given in Table 1, we have performed a Monte-Carlo test as described in Section 2.2 of Zong et al. (2016b), but specifically tuned to the *TESS* light curve of TIC 278659026 (i.e., using the exact same time sampling and parameters to compute the LSP). This allows us to evaluate probabilities that a peak at given S/N-values or above is real and not due to a random fluctuation of the noise. The test indicates that our lowest-S/N frequency retained, f_{23} with $S/N = 4.4$, has 99% chances to be real, while this probability goes above 99.99% (less than 1 chance out of 10,000 to be a false positive) for $S/N \gtrsim 5.1$. Since the frequency spectrum is very clean, in particular around the few frequencies below $S/N \sim 5$, we consider in the following analysis that even f_{23} is a securely established frequency of TIC 278659026 pulsation spectrum.

It is important to note that, while most frequencies in the LSP could be prewhitened without leaving any residual behind, thus indicating strong stability over the 27.88 days of observation, significant remaining peaks could be found at two occasions. The first case occurred for f_7 at 185.014 μHz which has f_{18} at 184.479 μHz as a closeby companion, considering that the formal frequency resolution in Fourier space for these data is 0.415 μHz ($1/T$, where T is the time baseline of the run). The other case is f_{14} at 245.609 μHz which has f_{20} at 245.102 μHz and f_{17} at 246.027 μHz as close neighbours. From a pulsation perspective, these frequencies could very well be real independent modes of different degree ℓ that happen to have very close frequen-

[5] Only data points without any warning flag are considered and no additional processing of the light curve is done.
[6] All L-S periodograms presented in this study are computed using oversampling by a factor of 7.
[7] This threshold follows common practice in the field, but significance of the lowest-S/N peaks is re-evaluated afterward.

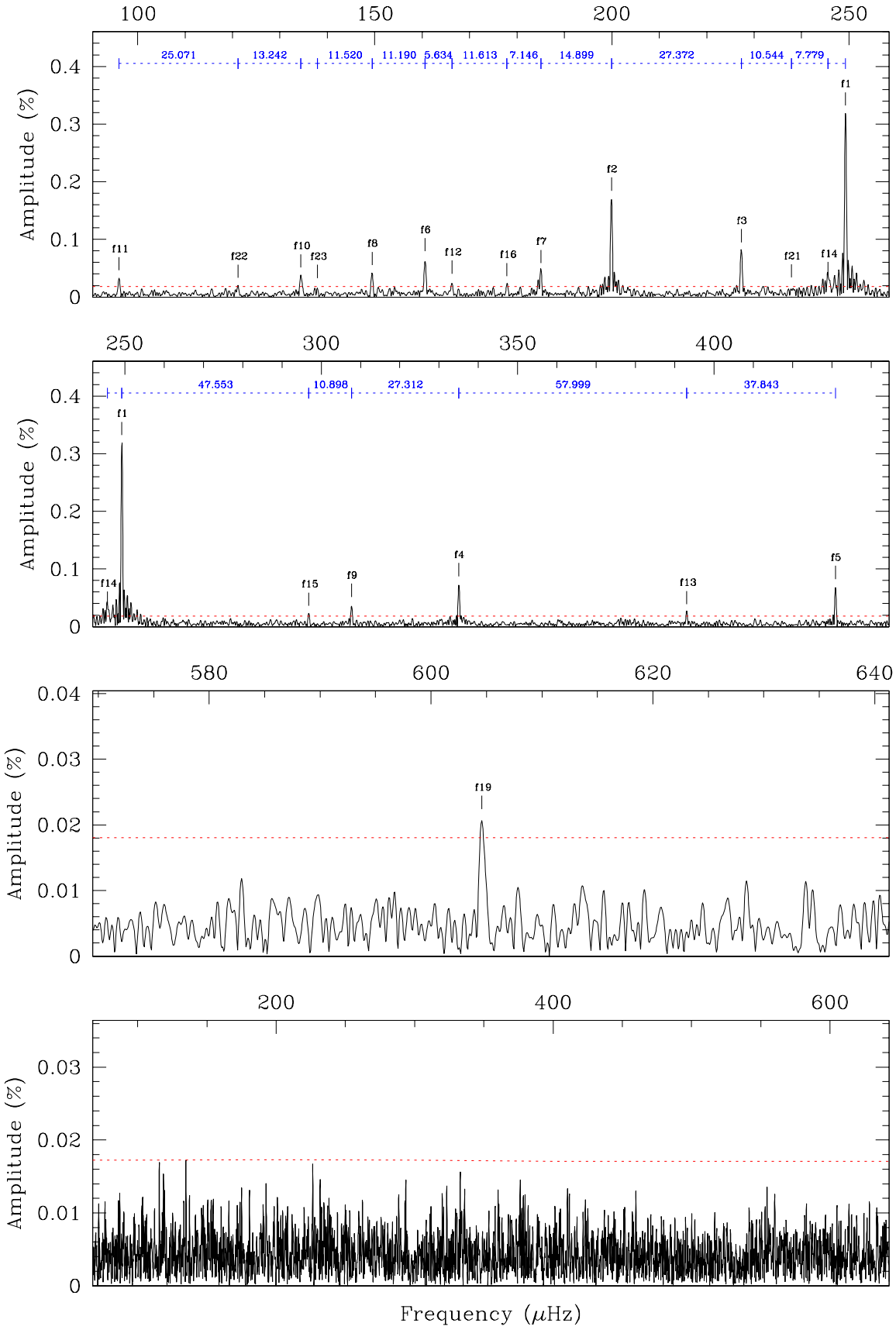

Fig. 3. The three upper panels show close-up views of the Lomb-Scargle Periodogram of TIC 278659026 in the g-mode frequency range. The main frequencies listed in Table 1 are indicated, except the three peaks (f_{18}, f_{17}, and f_{20}; see text). In the top two panels, the separation in frequency between two consecutive peaks is indicated (the horizontal dotted-line segments). The horizontal dotted line in each panel indicates 4 times the median noise level used as an initial significance criterion. The *Bottom panel* shows the residual after prewhitening all the frequencies.

Table 1. List of frequencies above 4 times de the median noise level extracted from TIC 278659026 light curve and their parameters. Each modulation is modeled as $f_i = A_i \cos[2\pi(\nu_i t + \phi_i)]$, where A_i, ν_i, and ϕ_i is the given amplitude, frequency, and phase, respectively. The phase is relative to a starting time $T_S = 1325.297922$ BJD, using 2457000 BJD as the reference date. Frequencies marked with a "*" are interpreted as independent pulsation modes and are used for the detailed asteroseismic analysis.

Id.		Frequency (μHz)	σ_f (μHz)	Period (d)	σ_P (d)	Amplitude (%)	σ_A (%)	Phase	$\sigma_{\rm Ph}$	S/N	Comments
f_A		1.563	0.019	7.407	0.088	0.0574	0.0047	0.300	0.017	12.3	Instr.?‡
f_B		3.173	0.035	3.648	0.040	0.0304	0.0047	0.031	0.015	6.5	Instr.?; $2f_A$‡
f_C		4.966	0.033	2.331	0.015	0.0324	0.0047	0.819	0.009	6.9	Instr.?‡
Id.		Frequency (μHz)	σ_f (μHz)	Period (s)	σ_P (s)	Amplitude (%)	σ_A (%)	Phase	$\sigma_{\rm Ph}$	S/N	Comments
f_{11}	*	96.073	0.030	10408.72	3.29	0.0324	0.0043	0.3310	0.0004	7.5	
f_{22}	*	121.144	0.051	8254.62	3.46	0.0194	0.0043	0.6661	0.0006	4.5	99.5% real signal†
f_{10}	*	134.387	0.026	7441.22	1.46	0.0375	0.0043	0.8808	0.0003	8.7	
f_{23}	*	137.912	0.052	7251.01	2.72	0.0192	0.0043	0.6056	0.0005	4.4	99% real signal†
f_8	*	149.432	0.024	6692.01	1.07	0.0416	0.0043	0.6680	0.0002	9.6	
f_6	*	160.622	0.015	6225.81	0.59	0.0655	0.0043	0.5316	0.0001	15.1	
f_{12}	*	166.256	0.037	6014.82	1.35	0.0266	0.0043	0.0062	0.0003	6.1	
f_{16}	*	177.869	0.044	5622.13	1.40	0.0223	0.0043	0.1369	0.0003	5.2	
f_{18}		184.479	0.046	5420.68	1.36	0.0214	0.0043	0.5000	0.0003	5.0	linked to f_7
f_7	*	185.014	0.022	5404.99	0.64	0.0452	0.0043	0.2034	0.0002	10.4	
f_2	*	199.913	0.006	5002.18	0.14	0.1706	0.0043	0.4374	0.0001	39.5	
f_3	*	227.285	0.012	4399.77	0.24	0.0810	0.0043	0.4979	0.0001	18.8	
f_{21}	*	237.829	0.049	4204.70	0.87	0.0200	0.0043	0.7711	0.0003	4.6	99.7% real signal†
f_{20}		245.102	0.047	4079.93	0.78	0.0210	0.0043	0.8531	0.0003	4.9	linked to f_{14}
f_{14}	*	245.609	0.041	4071.52	0.68	0.0240	0.0043	0.5993	0.0002	5.6	
f_{17}		246.027	0.045	4064.60	0.75	0.0219	0.0043	0.8582	0.0003	5.1	linked to f_{14}
f_1	*	249.269	0.003	4011.74	0.05	0.3184	0.0043	0.7808	0.0001	73.7	
f_{15}	*	296.822	0.044	3369.02	0.50	0.0224	0.0043	0.5569	0.0002	5.2	
f_9	*	307.720	0.026	3249.70	0.28	0.0377	0.0043	0.6263	0.0001	8.7	
f_4	*	335.033	0.013	2984.78	0.12	0.0735	0.0043	0.9914	0.0001	17.1	
f_{13}	*	393.032	0.039	2544.32	0.25	0.0251	0.0043	0.6513	0.0001	5.9	
f_5	*	430.875	0.014	2320.86	0.08	0.0686	0.0043	0.5398	0.0001	16.1	
f_{19}	*	604.580	0.046	1654.04	0.13	0.0212	0.0043	0.7714	0.0001	5.0	

‡These signals are difficult to interpret. Intrumental artifacts of yet unclear origin may be present in this frequency range and contamination from a bright nearby object, TIC 278659026 (TYC 9327-275-1), cannot be excluded.
†Evaluated from a specific Monte-Carlo test as described in Zong et al. (2016b).

cies, barely resolved with the current data set. However, they may also be the signature of intrinsic modulations (of amplitude and/or frequency) of the dominant peak, as discussed by Zong et al. (2016b,a, 2018). Therefore, as a precaution, we will retain only the main (highest amplitude) peak of each complex, namely f_7 and f_{14}, for the detailed asteroseismic study of TIC 278659026.

Finally, we emphasize from Table 1 a few numbers characterizing the quality of these first *TESS* data obtained on a pulsating hot B subdwarf star. With only one sector (27.88 days), targeting a rather bright ($V = 11.57$), hot and blue object, the amplitude of the noise in Fourier space is around 0.0043% (43 ppm) in the g-mode frequency range, which is a remarkable achievement. One can expect this noise to be reducted further by up to a factor of ~ 3.5 for similar targets located in or near the Continuous Viewing Zone, that could be observed for up to one year. We also note that the precision on the measured frequencies is typically around one-tenth of the formal frequency resolution.

3. Asteroseismic analysis

3.1. Interpretation of the observed spectrum

Figure 3 shows a pulsation spectrum whose frequency distribution is quite typical of g-mode pulsators observed from space. The frequency spacings between consecutive peaks do not show quasi-symmetric structures that could clearly correspond to the signature of rotational splitting. Yet, one could argue that the projected rotational velocity of ~ 8 km.s^{-1} proposed for TIC 278659026, if true (see Sect. 2.1), would correspond, for a star of radius 0.15 $R_\odot$, to a rotation period that is slightly less than a day. Assuming a median statistical inclination of 60°, this period would be ~ 0.82 day, and the corresponding splittings ~ 7 μHz

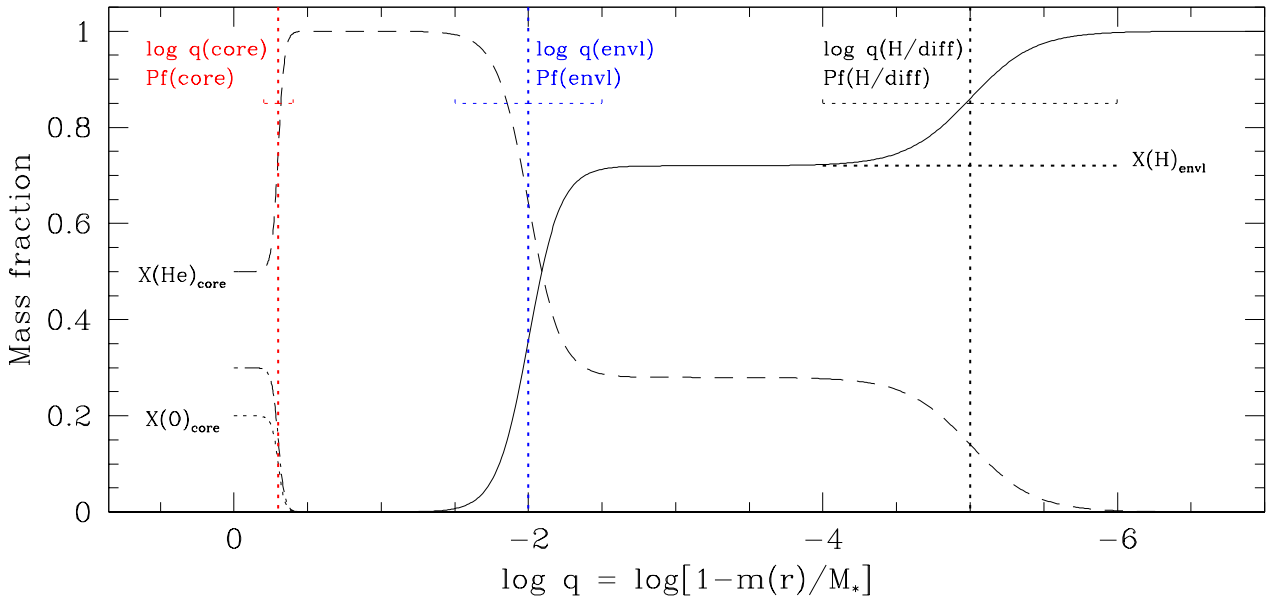

Fig. 4. Illustration of the model parameters specifying the chemical stratification (see text for a full description of these parameters). The plain (dashed, dotted-dashed, and dotted) curve corresponds to the hydrogen (helium, carbon, and oxygen) mass fraction as a function of fractional mass depth, $\log q$.

for dipolar ($\ell = 1$) g-modes and ~ 11 μHz for quadrupolar ($\ell = 2$) g-modes. Values close to these splittings can be seen between some of the observed peaks, but without the regularity that usually characterizes splittings at such slow rotation rates. Moreover, the typical average period spacings between consecutive g-modes of same degree in sdB stars generate frequency spacings, in the range where these pulsations are observed, that are also of the same order, without invoking rotation. To help in choosing between these two very different interpretations of the spectrum, it is important to recall that a still unexplained discrepancy exists between the typical rotation rates inferred for sdB stars from spectroscopy (Geier et al. 2010; Geier & Heber 2012) and the rotation periods measured from well-identified rotational splittings observed in pulsating sdB stars, in particular in those with very long time series delivered by the *Kepler* satellite (see, e.g., Kern et al. 2017 and other references provided in Charpinet et al. 2018). These splittings indeed indicate in a quite robust way that nearly all sdB pulsators, in particular the single ones, are extremely slow rotators with periods typically well above 10 days, at odd with the average ~ 1 day periods found by Geier & Heber (2012). Asteroseismology clearly is much more sensitive to very slow rotation rates than line broadening analyses, and the question then arises whether the ~ 8 km.s^{-1} projected velocity found to be typical of sdB stars, which is not far above the limit of this method with the available spectra, is an actual measurement of the surface rotation of the star, an upper limit of it, or reflects an effect other than rotation causing additional broadening of the metal lines that has not been taken into account. This issue is well beyond the scope of the present paper, but clearly needs further investigation, possibly with the acquisition and analysis of very high resolution spectra for a selection of pulsating and nonpulsating hot B subdwarf stars.

For the present seismic study of TIC 278659026, we rely on previous observations of pulsating sdB stars, indicating extremely slow rotation rates, and we interpret 20 observed frequencies (those marked with a "*" sign in Table 1) as independent sectoral ($m = 0$) g-modes of degree $\ell = 1$ or $\ell = 2$. The first assumption follows from the above discussion and is further justified by the fact that the time baseline of the *TESS* run would likely be too short to resolve eventual $m \neq 0$ components in this framework. The observed frequencies can therefore be compared with the model frequencies computed assuming a nonrotating star, without any impact on the solution. The second assumption limits our search to dipole ($\ell = 1$) and quadrupole ($\ell = 2$) modes only, and is justified by the fact that cancellation effects over the stellar surface very strongly reduce the apparent amplitude of $\ell > 2$ g-modes in sdB stars, except for very specific inclination angles of the pulsation axis relative to the line of sight. This has been clearly illustrated in Figure 11 of Charpinet et al. (2011), which shows that $\ell = 3, 4$ modes have apparent amplitudes already reduced by a factor of at least 10 due to this effect. Such modes are therefore much less likely to be seen in the current data.

3.2. Method and models

The asteroseismic analysis of TIC 278659026 is based on the forward modelling approach developed over the years for hot-subdwarf and white-dwarf asteroseismolology and described in, e.g., Charpinet et al. (2005, 2008); Van Grootel et al. (2013); Charpinet et al. (2014c, 2015); Giammichele et al. (2016). The method is a multi-dimensional optimization of a set of parameters defining the stellar structure of the star with the goal to minimize a "merit function" that measures the ability of that model to reproduce *simultane-*

ously all the observed pulsation frequencies. In the present analysis, the quality of the fit is quantified using a χ^2-type merit function defined as

$$S^2(p_1, ..., p_n) = \sum_i^{N_{\rm obs}} \left(\frac{\nu_{{\rm obs},i} - \nu_{{\rm th},i}}{\nu_{{\rm obs},i}} \right)^2 \quad ,$$

where $N_{\rm obs}$ is the number of observed frequencies and $(\nu_{{\rm obs},i}, \nu_{{\rm th},i})$ is a pair of associated observed/computed frequencies. We recall that this quantity, S^2, is minimized both as a function of the frequency associations, referred to as the first combinatorial minimization required because the observed modes are not identified *a priori*, and as a function of the model parameters, $\{p_1, ..., p_n\}$ (the second minimization). This optimization is carried out by the code LUCY, a Real-Coded Genetic Algorithm (RCGA) that can pursue multimodal optimization (i.e., searching simultaneously for multiple solutions) in any given multi-dimensional parameter space. This optimizer is coupled with a series of codes dedicated to the computation of the stellar structure itself (given a set of parameters) and its pulsation properties, as well as to the matching of the computed frequencies with the observed ones.

Our current version of stellar models used for quantitative asteroseismology of sdB stars is an evolution of the Montréal so-called "third-generation" (3G) models designed for an accurate computation of g-mode frequencies (Brassard & Fontaine 2008, 2009; Van Grootel et al. 2010a; Charpinet et al. 2011). These models are complete hydrostatic stellar structures in thermal equilibrium computed from a set of parameters that define the main structural properties of the star. The implemented parametrization is inspired from full evolutionary calculations, which provide the guidelines to reproduce, e.g., the general shape of the composition profiles in these stratified stars, but with additionnal flexibility. We recall that the reasons why we rely on parametrized static structures are both technical, as such models are much more versatile and faster to compute than evolutionary structures, and strategic, since they greatly enhance our capacity to explore a multitude of structural configurations in the spirit of extracting constraints from the pulsation modes themselves. The derived optimized structures are therefore seismic models that are mostly independent of the uncertainties still present in the physics that drives stellar evolution.

Compared to the former 3G models used in, e.g., Van Grootel et al. (2010a,b); Charpinet et al. (2011); Van Grootel et al. (2013), the most important improvement is that our current stellar structures for sdB stars now implement a more realistic hydrogen-rich envelope with a double-layered hydrogen/helium composition profile. This addition was motivated by the fact that diffusion of helium through gravitational settling does not have the time, during the typical duration of the core helium burning phase, to completely sink below the envelope when this envelope is relatively thick (see, e.g., Hu et al. 2009, 2010). This is most likely to be relevant for g-mode sdB pulsators that are found among the cooler sdB stars having thicker envelopes, while the hotter p-mode sdB pulsators all have thinner envelopes that quickly become fully hydrogen-pure. Consequently, in the present analysis, the assumption of a pure hydrogen envelope used so far is better replaced by an envelope which may still contain some helium, with a transition from pure hydrogen (at the top) to a mixture of H/He (at its base). The technical implementation of this double-layered He/H composition profile is identical in its principle to the implementation of a double-layered helium envelope in DB white dwarf models, as described recently in the Methods section of Giammichele et al. (2018).

The input parameters needed to fully define the stellar structure with these improved models are the following. First the total mass, M_*, of the star has to be given. All additional parameters specify the chemical stratification inside the star, as illustrated in Fig. 4. We start with five parameters defining the double-layered He/H envelope structure. The first one is the fractional mass of the outer hydrogen-rich envelope, $\log q({\rm env}) = \log(M_{\rm env}/M_*)$, corresponding in effect to the location of the deepest transition of the double-layered structure, from the pure He mantle to the mixed He/H region at the bottom of the envelope. The second one is the fractional mass of the pure hydrogen layer at the top of the envelope, $\log q({\rm H/diff}) = \log(M_{\rm H/diff}/M_*)$, which fixes the location of the transition between the He/H mixed layer to the pure hydrogen region. The shape (or extent) of both transitions are controled by two additional parameters, $Pf({\rm envl})$ and $Pf({\rm H/diff})$ (see the Methods section of Giammichele et al. 2018 for details). The remaining parameter, $X({\rm H})_{\rm envl}$, closes the specification of the envelope structure by fixing the mass fraction of hydrogen in the mixed He/H region of the envelope. We also note for completeness that the stellar envelope incorporates a non-uniform iron distribution computed assuming equilibrium between radiative levitation and gravitational settling (see Charpinet et al. 1997, 2001). In addition to this set of parameters, the core structure has to be defined by specifying the fractional mass of the convectively mixed core, $\log q({\rm core}) = \log(M_{\rm core}/M_*)$, which sets the position of the transition between the CO-enriched core (due to helium burning) with the surrounding helium mantle. How steep (or wide) is this transition is specified by the profile factor, $Pf({\rm core})$, and the composition of the core is determined by the two parameters $X({\rm He})_{\rm core}$ and $X({\rm O})_{\rm core}$ providing the mass fraction of helium and oxygen (the complement being carbon with $X({\rm C})_{\rm core} = 1 - X({\rm He})_{\rm core} - X({\rm O})_{\rm core}$). A full sdB stellar structure is therefore entirely specified with the 10 "primary" parameters mentionned above. Other "secondary" quantities that can be of specific interest, such as the effective temperature, surface gravity, or stellar radius simply derives from the converged stellar model in hydrostatic and thermal equilibrium.

Finally, we recall that the seismic properties of a given stellar model are computed using a modern version of the Montréal pulsation code (Brassard et al. 1992; Brassard & Charpinet 2008). Calculations in the adiabatic approximation are sufficient for the pursued purposes and much more efficient numerically than the full non-adiabatic treatment.

3.3. Search for an optimal seismic model

The search for an optimal solution that reproduces the seismic properties of TIC 278659026 was conducted in the multi-dimensional space defined by the 10 primary model parameters discussed in the previous subsection. A first exploratory optimization with the code LUCY was performed to cover the largest possible domain in parameter space, relevant for virtually all configurations that could potentially correspond to a hot B subdwarf star. This

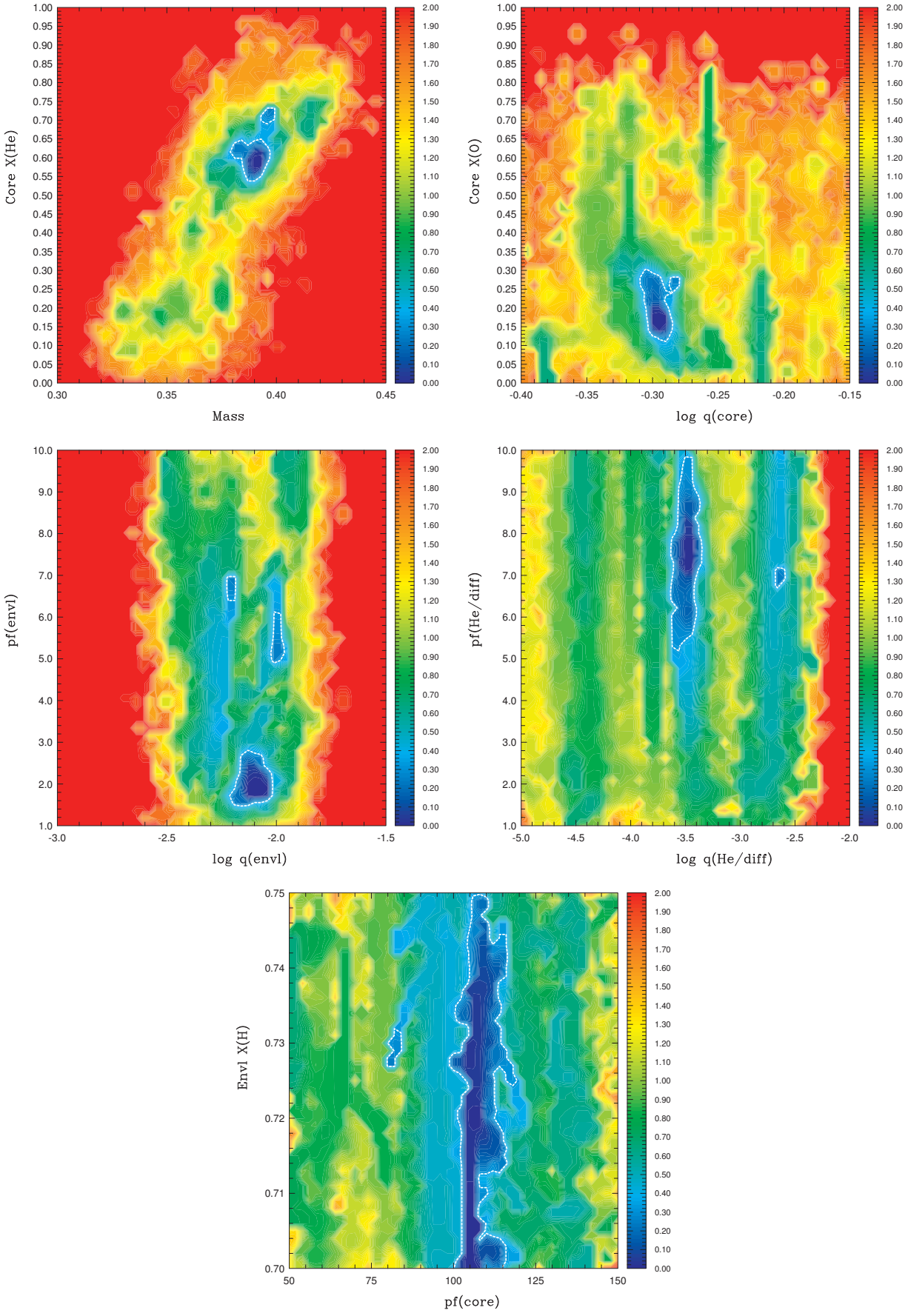

Fig. 5. $\log S^2$-projection maps for pairs of primary model parameters showing location and shape of best-fitting regions in parameter space (see text for more details). Note that S^2 is normalized to one at minimum and the color scale is logarithmic. Dark blue indicates the best-fit regions and the dotted contour line is an estimate of the 1σ-confidence level, obtained similarly as described in Brassard et al. (2001).

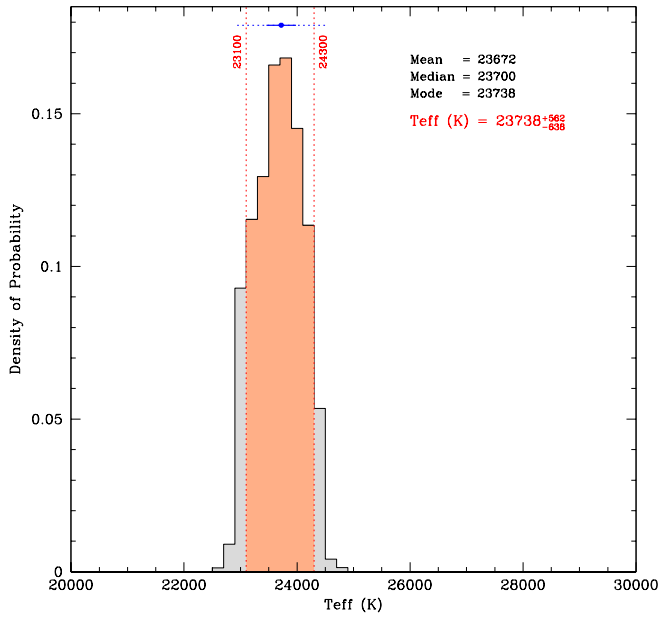

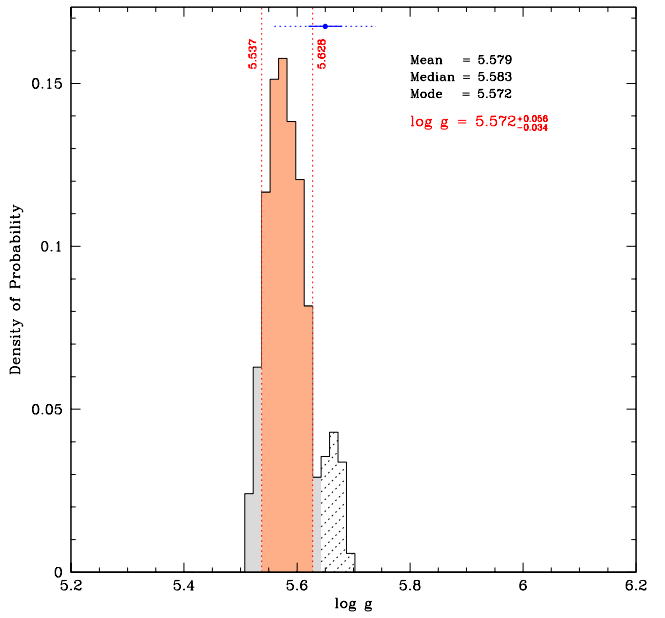

Fig. 6. Probability distribution for $T_{\rm eff}$ (*top panel*) and $\log g$ (*bottom panel*) around the optimal seismic solution for TIC278659026. Red-shaded areas contains 68% of the distribution and provide the 1σ error range for the considered quantity. For internal physical consistency of the derived parameters, the adopted value is the mode (maximum) of the distribution, which corresponds to the value of the optimal model. Note that when a weaker secondary peak exists in the distribution (e.g., in *bottom panel*), the evaluation of the 1σ boundaries is limited to the main structure associated with the optimal model solution. In such cases, the excluded parts of the distribution are shown as hatched areas. The blue dots, and their associated horizontal lines, indicate the measurement obtained independently from spectroscopy, and the 1σ (solid) and 3σ (dotted) ranges around that value.

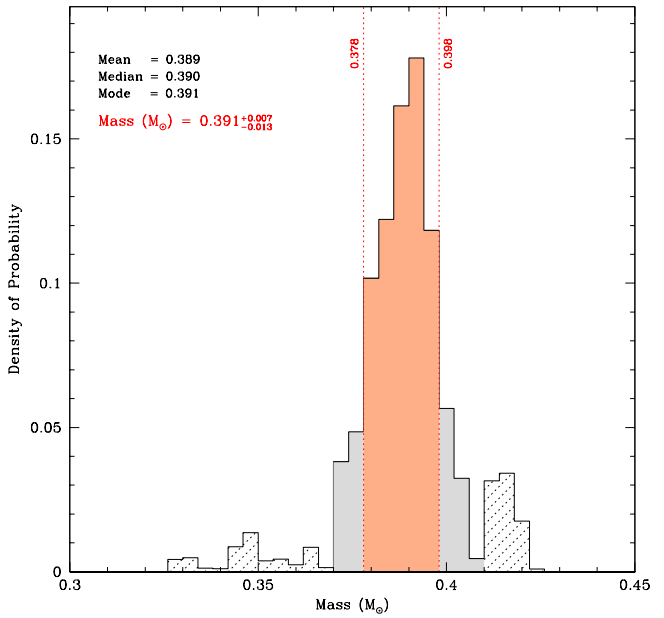

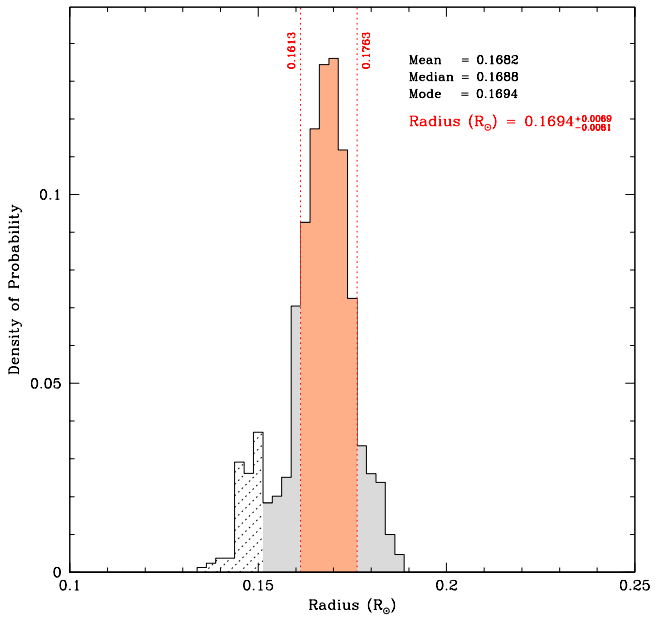

Fig. 7. Same as Figure 6 but for the mass (*top panel*) and radius (*bottom panel*) of TIC278659026.

wide domain was delimited by $0.30 \leq M_*/M_\odot \leq 0.60$, $-10.0 \leq \log q({\rm H/diff}) \leq -2.0$, $-4.0 \leq \log q({\rm envl}) \leq -1.5$, $-0.5 \leq \log q({\rm core}) \leq -0.1$, $0.0 \leq X({\rm He})_{\rm core} \leq 1.0$, $0.0 \leq X({\rm O})_{\rm core} \leq 1.0$, $0.70 \leq X({\rm H})_{\rm envl} \leq 0.75$, $1 \leq {\rm Pf(H/diff)} \leq 10$, $1 \leq {\rm Pf(envl)} \leq 10$, $1 \leq {\rm Pf(core)} \leq 150$, and the search was done without considering at this stage the constraint available from spectroscopy. Remarkably, this first calculation pointed toward a basin of solutions located very close to the spectroscopic values of $\log g$ and $T_{\rm eff}$, suggesting a sdB star of relatively low-mass. This helped to reducee the size of the search space for the ultimate convergence toward the best-fit solution.

The second and ultimate round of optimization was conducted within the ranges $0.30 \leq M_*/M_\odot \leq 0.45$, $-5.0 \leq \log q({\rm H/diff}) \leq -2.0$, $-3.0 \leq \log q({\rm envl}) \leq -1.5$,

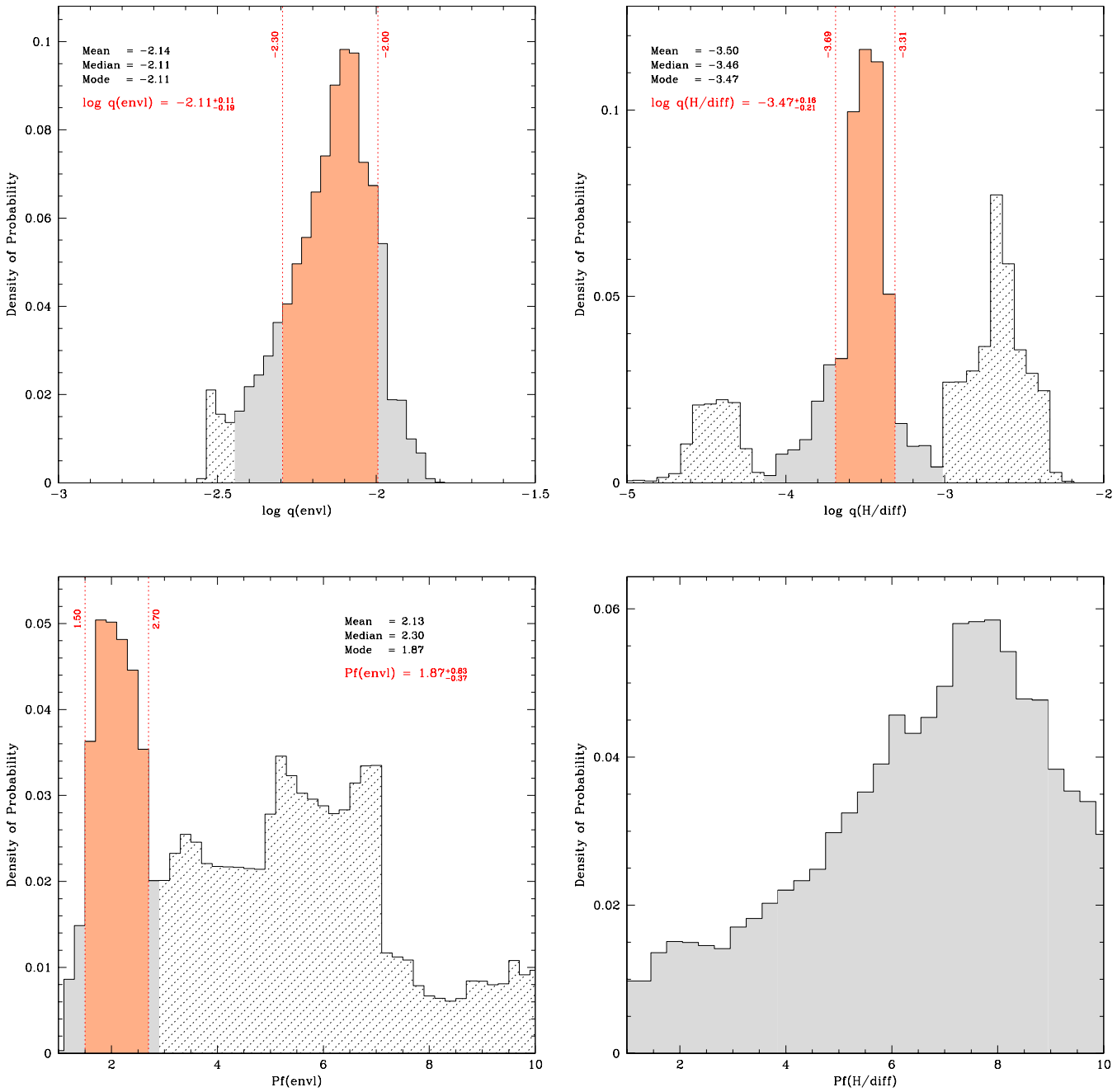

Fig. 8. Same as Figure 6 but for the remaining envelope structural parmameters defining the seismic model of TIC278659026.

$-0.40 \leq \log q(\mathrm{core}) \leq -0.15$, $0.0 \leq X(\mathrm{He})_{\mathrm{core}} \leq 1.0$, $0.0 \leq X(\mathrm{O})_{\mathrm{core}} \leq 1.0$, $0.70 \leq X(\mathrm{H})_{\mathrm{envl}} \leq 0.75$, $1 \leq \mathrm{Pf(H/diff)} \leq 10$, $1 \leq \mathrm{Pf(envl)} \leq 10$, $50 \leq \mathrm{Pf(core)} \leq 150$. This time the spectroscopic values of $\log g$ and T_{eff} were introduced in the optimization process as additional external constraints degrading progressively the merit function when a computed model has $\log g$ and/or T_{eff} that differ from spectroscopy by more than a tolerance range set to be 3σ (3 times the spectroscopic error). The optimizer LUCY was configured to agressively converge each potential model solution found in parameter space by combining the GA search with a simplex optimization round. This step ensures that the global and eventual local minima of the merit function are effectively reached. This second round of calculation required the computation and comparison with TIC 278659026 frequencies of 1,555,425 seismic models[8].

3.4. Seismic solution for TIC 278659026

The first result emerging from the optimization in the 10-dimensional parameter space is the identification of a solution for TIC 278659026 that clearly dominates over other secondary options. This is illustrated in Fig. 5, showing the

[8] This calculation was performed on the high-performance cluster OLYMPE at the CALMIP computing center using 480 CPU cores in parallel for approximately 3 days.

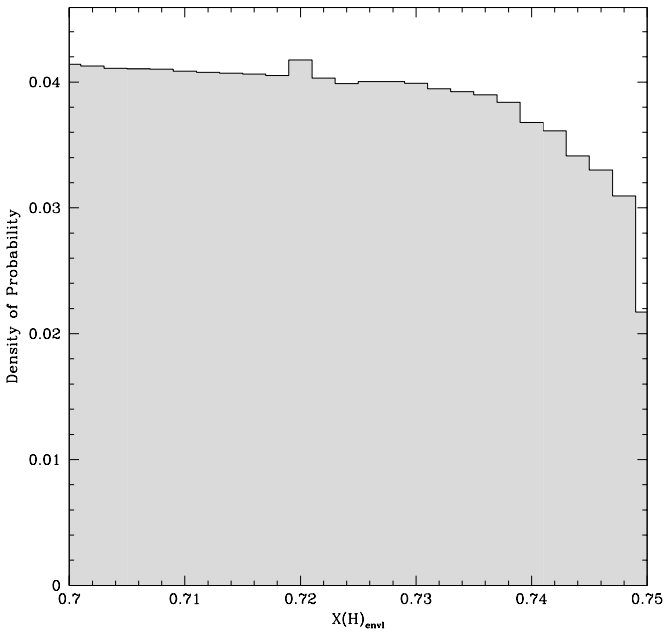

Fig. 9. Same as Figure 8 but for the mass fraction of hydrogen, $X(\mathrm{H})_{\mathrm{envl}}$, at the bottom of the hydrogen-rich envelope.

2D projection maps of $\log S^2$ (S^2 being normalized to one at minimum in this context) for the various pairs of input parameters defining the models. The approximate reconstruction of the topology of S^2 derives from the sampling of the merit function by the optimizer during the search. While $\log S^2$ has a rather complex structure with several local dips, as expected, a dominant global minimum is found. Moreover, all parameters appear rather well constrained (i.e., precisely localized around the optimum), except for the hydrogen content in the mixed He/H region at the based of the envelope, $X(\mathrm{H})_{\mathrm{envl}}$, whose minimum is an elongated valley.

The identification of a well-defined global minimum dominating all the other optima allows for the selection of an optimal seismic model of TIC 278659026 and a quantitative assertion of its parameters through the series of plots provided in Fig. 6, 7, 8, 9, and 10. These histograms show the probability distributions for the most relevant parameters through marginalization. As described in, e.g., Van Grootel et al. (2013), these distributions are evaluated from the likelihood function ($\propto e^{-\frac{1}{2}S^2}$) and are useful to estimate the internal error associated with each parameter value. Here, slightly varying from previous similar studies, the derived parameters are given by the mode (maximum) of their corresponding distribution, which ensures internal physical consistency between all values, since they represent the optimal seismic model. We point out that for histograms differing significantly from the normal distribution, for instance when secondary peaks are visible, we chose to estimate these errors relative to the distribution in the close vicinity of the dominant solution. All the values derived from the optimal seismic model and their estimated errors are provided in Table 2, along with other independent measurements of the same quantity when available, for comparison purposes.

3.4.1. Global parameters

Table 2. Derived properties of TIC 278659026.

Quantity	Value derived from seismology	Other Measurement
Primary quantities[a]		
$M_*/M_\odot$	0.391 ± 0.013	$0.39 \pm 0.09^{\ddagger}$
$\log q(\mathrm{env})$	-2.11 ± 0.19	...
$\log q(\mathrm{H/diff})$	-3.47 ± 0.21	...
$X(\mathrm{H})_{\mathrm{envl}}$	~ 0.72	...
Pf(envl)	1.87 ± 0.83	...
Pf(H/diff)	~ 7.7	...
$\log q(\mathrm{core})$	-0.295 ± 0.018	...
Pf(core)	107 ± 12	...
$X(\mathrm{He})_{\mathrm{core}}$	$0.57^{+0.08}_{-0.03}$	...
$X(\mathrm{O})_{\mathrm{core}}$	$0.16^{+0.13}_{-0.07}$	...
Secondary quantities[b]		
T_{eff} (K)	23740 ± 640	23720 ± 260^{c}
$\log g$	5.572 ± 0.056	5.650 ± 0.030^{c}
$R/R_\odot$	0.1694 ± 0.0081	...
$M_{\mathrm{H}}/M_\odot$	$0.0037 \pm 0.0017^{\dagger}$	...
$M_{\mathrm{core}}/M_\odot$	0.198 ± 0.015	...
$X(\mathrm{C})_{\mathrm{core}}$	$0.27^{+0.08}_{-0.15}$	...
$L/L_\odot$ (T_{eff}, R)	8.2 ± 1.7	8.2 ± 1.1^{c}
M_V (g, T_{eff}, M_*)	4.92 ± 0.15^{d}	...
M_{B_p} (g, T_{eff}, M_*)	4.70 ± 0.16^{d}	...
$(B\text{-}V)_0$	-0.225 ± 0.007^{d}	...
$(B_p\text{-}R_p)_0$	-0.404 ± 0.011^{d}	...
V	...	11.57 ± 0.09^{e}
$(B\text{-}V)$	...	-0.22 ± 0.10^{e}
B_p	...	11.433 ± 0.008^{f}
$(B_p\text{-}R_p)$	...	-0.398 ± 0.009^{f}
$E(B\text{-}V)$	0.005 ± 0.107	...
$E(B_p\text{-}R_p)$	0.005 ± 0.020	...
d_{parallax} (pc)	...	203.7 ± 2.1^{g}
d_V (pc)	212.2 ± 57.0^{h}	...
d_{B_p} (pc)	220.9 ± 20.4^{i}	...

[a] Optimized model parameters (see text)
[‡] From fitting the SED and using *Gaia* DR2 parallax (see text)
[b] Quantities derived from the computed models
[c] From spectroscopy (Németh et al. 2012)
[†] $\log \frac{M(\mathrm{H})}{M_*} = \log q(\mathrm{envl}) + C = -2.0251$; C comes from the model
[d] From a model atmosphere with $\log(\frac{\mathrm{He}}{\mathrm{H}}) = -3.0$
[e] from Høg et al. 2000
[f] from *Gaia* DR2 photometry
[g] From *Gaia* DR2 parallax, $\varpi = 4.910 \pm 0.051$ mas
[h] $d = 213.8 \pm 23.4$ without correction for extinction
[i] $d = 221.9 \pm 16.6$ without correction for extinction

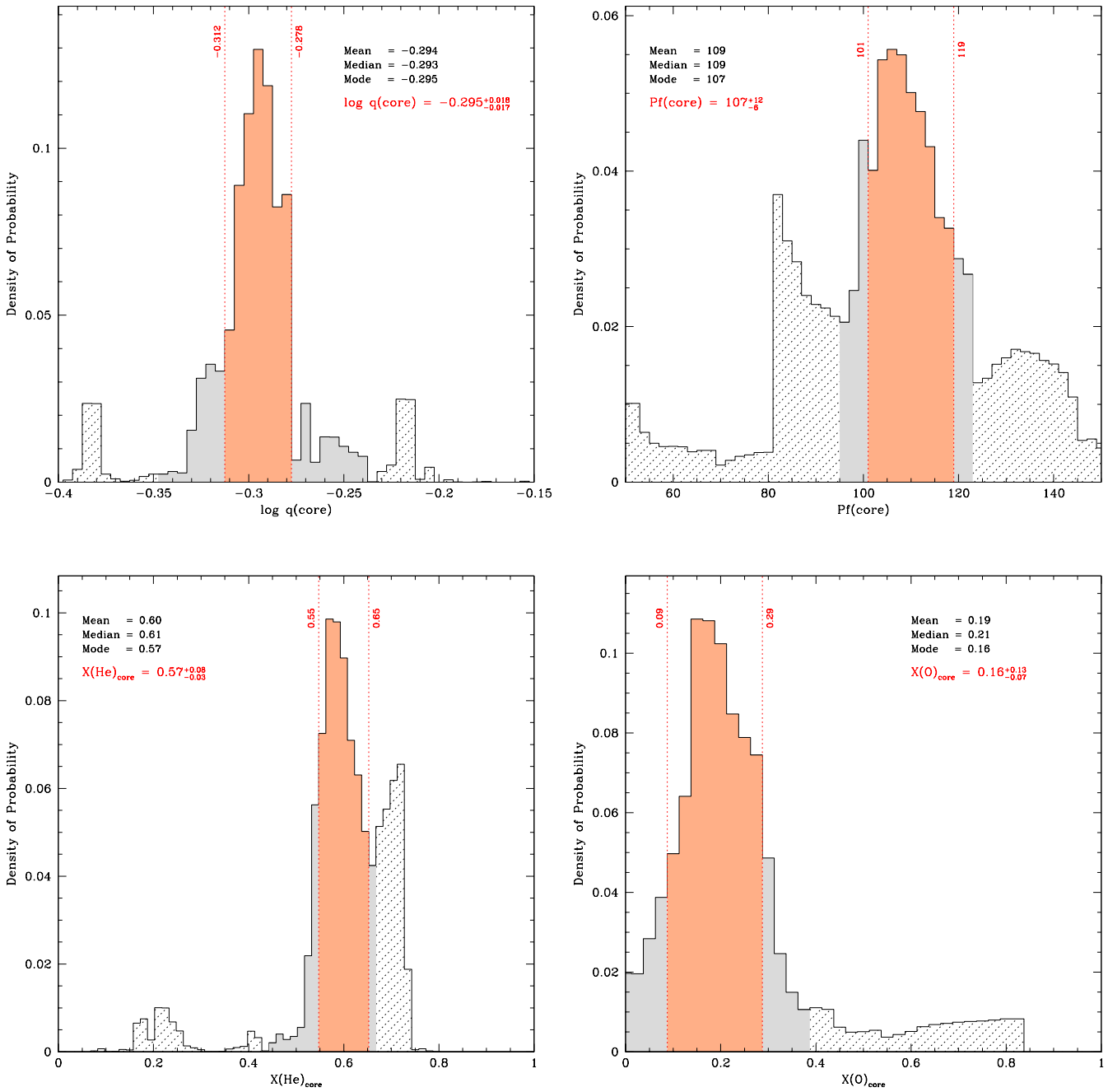

Fig. 10. Same as Figure 6 but for the core structural parmameters defining the seismic model of TIC278659026.

The seismic model uncovered for TIC 278659026 has $T_{\rm eff}$ and $\log g$ values in very close agreement – both within or very close to the 1σ error bars – with the values measured independently from spectroscopy (Fig. 6). This demonstrates a remarkable consistency of the solution that was not guaranteed *a priori*. We also find that TIC 278659026 has a tightly constrained radius of 0.1694 ± 0.0081 $R_\odot$ and a mass of 0.391 ± 0.013 $M_\odot$ (Fig. 7). The latter is significantly less than the canonical mass of ~ 0.47 $M_\odot$ expected for typical hot B subdwarf stars, which indeed explains why TIC 278659026 has a rather high surface gravity (and small radius) given its relatively low effective temperature, that places it somewhat below the bulk of hot subdwarfs in a $\log g - T_{\rm eff}$ diagram. It is the first g-mode pulsating sdB star (and only second pulsator, if we include the *V361 Hya* stars) with such a low mass determined precisely from asteroseismology. Therefore, this object bears a particular interest in the context of determining the empirical mass distribution of field sdB stars (see, Fontaine et al. 2012).

A second important test of the reliability of the seismic solution is provided by the comparison, in Table 2, between the distance of the star measured from the available *Gaia* DR2 trigonometric parallax and the "seismic distance" evaluated from the optimal model properties. The latter is obtained by computing a representive model atmosphere of TIC 278659026 from the parameters of the seismic model,

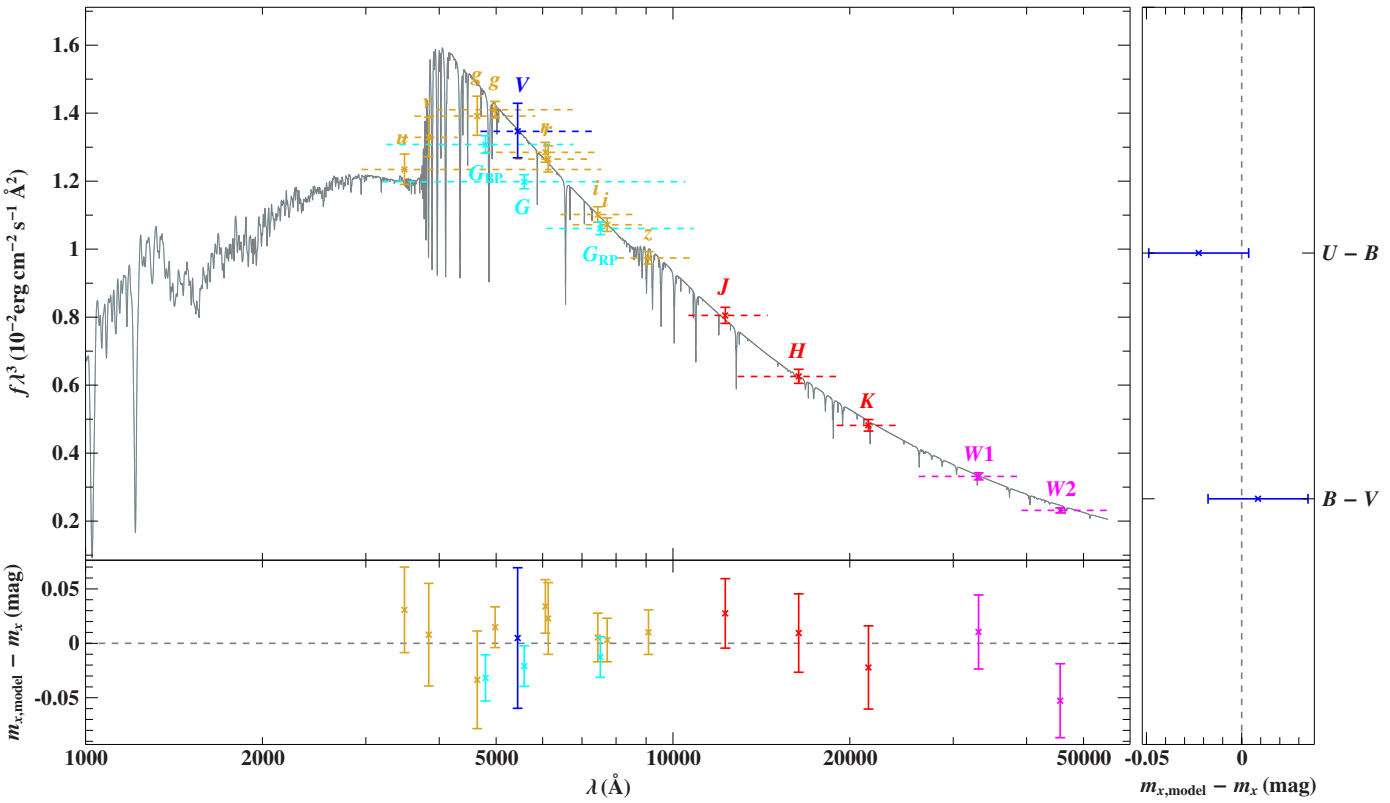

Fig. 11. Comparison of synthetic and observed photometry: The *top panel* shows the spectral energy distribution. Colored data points represent the filter-averaged fluxes, which were converted from observed magnitudes (the respective filter width is indicated by dashed horizontal lines), while the gray solid line represents a synthetic spectrum computed from a model atmosphere using the atmospheric parameters from Németh et al. (2012). The panels at the bottom and on the right hand side show the differences between synthetic and observed magnitudes/colors. The following color codes are used to identify the photometric systems: Johnson (blue), APASS g, r, i (yellow), SkyMapper (yellow), *Gaia* (cyan), 2MASS (red), and WISE (magenta).

used to derive absolute magitudes and theoretical color indices in the photometric band-passes of interest. Combined with photometric measurements, these values give access to estimates of the interstellar reddening and ultimately to the distance modulus (corrected by the extinction, found to be almost negligible in the present case). We find that the seismic distance obtained for TIC 278659026 is in very close agreement – compatible with 1σ errors – with the distance measured by *Gaia*. This indicates that the global properties of the star obtained from our seismic analysis, in particular its effective temperature, mass, and radius, are indeed accurate to the quoted precision.

As a last complementary check, we derive interstellar extinction from the spectral energy distribution (SED) and colors by comparing all available photometric measurements for TIC 278659026 to synthetic ones calculated from an appropriate model atmosphere (see Fig. 11). The photometry used in Fig. 11 (see Table 3) covers from the u-band to the infrared J, H, K (2MASS; Skrutskie et al. 2006) and $W1$, $W2$ (WISE; Cutri & et al. 2013). The Johnson V magnitude and colors for this specific test were taken from O'Donoghue et al. (2013). The SkyMapper (Wolf et al. 2018), APASS g, r, i (Henden et al. 2016), and *Gaia* (Gaia Collaboration et al. 2018) magnitudes were also included. Details of the model spectra and the fitting procedure are given by Heber et al. (2018). The angular diameter obtained from this fit is $\theta = \left(3.42^{+0.05}_{-0.06}\right) \times 10^{-11}$ and interstellar redding is found to be zero (i.e., E(B-V) ≤ 0.009; consistent with the value given in Table 2). This approach also esti-

Table 3. List of the observed magnitudes used to fit the SED (see Fig. 11).

System	Bandpass	Magnitude
Gaia	G	11.5928 ± 0.0009
Gaia	GRP	11.8308 ± 0.0018
Gaia	GBP	11.4327 ± 0.0083
WISE	W1	12.413 ± 0.023
WISE	W2	12.512 ± 0.023
2MASS	J	12.152 ± 0.021
2MASS	H	12.264 ± 0.025
2MASS	K	12.375 ± 0.027
SDSS	g	11.387 ± 0.033
SDSS	r	11.792 ± 0.022
SDSS	i	12.144 ± 0.010
Johnson	B-V	-0.23
Johnson	U-B	-0.89
Johnson	V	11.62
SkyMapper	u	11.283 ± 0.028
SkyMapper	v	11.309 ± 0.035
SkyMapper	g	11.444 ± 0.002
SkyMapper	r	11.767 ± 0.013
SkyMapper	i	12.208 ± 0.006
SkyMapper	z	12.521 ± 0.007

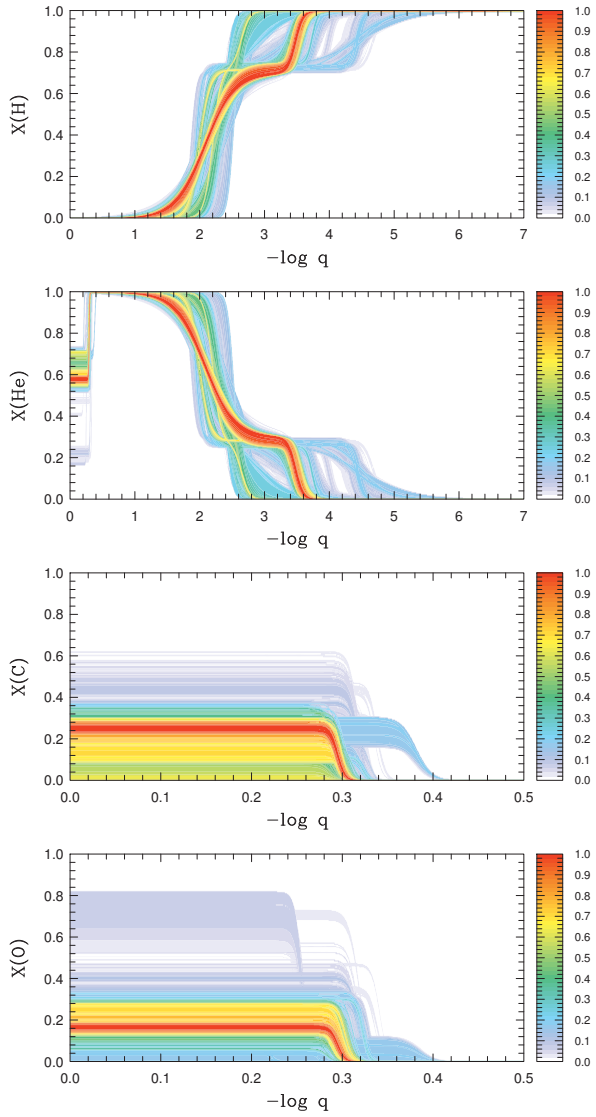

Fig. 12. Probability distributions (color scale) normalized to one at maximum as functions of the fractional mass depth, $\log q = \log[1 - m(r)/M_\star]$, obtained, from *top* to *bottom*, for the mass fraction of hydrogen, helium, carbon, and oxygen inside TIC 278659026. The red areas indicate the values, as functions of $\log q$, corresponding to the best matching seismic models. These distributions are derived from the evaluation of more the 1,555,425 stellar models calculated during exploration of parameter space.

mates a photometric effective temperature which is in perfect agreement with other methods, giving $T_{\rm eff} = 23600^{+700}_{-400}$ K. Using the high-precision parallax provided by *Gaia* DR2, $\varpi = 4.910 \pm 0.051$, combined with the angular diameter and the surface gravity, the stellar mass can be obtained through the relation $M = g\,\Theta^2/(4G\,\varpi^2)$. This results in a mass of $M = 0.39 \pm 0.09\ M_\odot$, based on the atmospheric parameters from Németh et al. (2012) using a conservative estimate of 0.1 dex for the error on $\log g$, instead of the statistical uncertainties quoted by the authors. This value is remarkably consistent with the mass derived from the asteroseismic solution. We close this discussion by noting that, interestingly, the WISE W2 measurement rules out the presence of a companion earlier than type M5/M6 (assuming a 3σ excess at W2 above the expected sdB photosphere).

3.4.2. Internal structure

Beyond the determination of the fundamental parameters characterizing TIC 278659026, our asteroseismic analysis provides insight on the internal structure of the star, in particular its chemical composition and stratification. Interesting constraints on the double-layered envelope structure are indeed obtained (Fig. 8, 9 and Table 2), along with measurements of the helium-burning core properties (Fig. 10 and Table 2). The various parameters defining these structures fully determine the chemical composition distribution inside the star for the 4 main constituants H, He, C, and O, and Fig. 12 provides a more convenient way to visualize these profiles and their uncertainties. This plot is constructed from the composition profiles in the 1,555,425 models evaluated by the optimizer during its exploration of the parameter space (see Giammichele et al. 2017 that introduced similar plots in a white dwarf context). Each model (and therefore each composition profile) has a S^2-value attributed regarding its ability to match the pulsation frequencies of TIC 278659026. Consequently, probability distributions for the amount of H, He, O, and C (the complement of He and O in the core) as functions of the fractional mass depth, $\log q = \log(1 - m(r)/M_*)$, can be evaluated. We find from these distributions that a well-defined region corresponding to best-fitting models emerge for each element, thus materializing the chemical stratification of TIC 278659026 as estimated from asteroseismology. Significantly weaker secondary solutions can also be seen in these diagrams.

From the obtained seismic solution, we find that TIC 278659026 has a rather thick envelope, with $\log q({\rm envl}) = -2.11 \pm 0.19$, with a remaining double-layered structure for the He/H profile indicating that gravitational settling has not completely segregated hydrogen from helium yet. Such a configuration is indeed expected for a cool sdB star such as TIC 278659026. The mass fraction of hydrogen present in this mixed He/H region should be close to the proportion expected in the solar mixture, since the sdB envelope should be the remain of the original main sequence stellar envelope. However, its exact value is not really constrained by our fit, although our optimal seismic model gives $X({\rm H})_{\rm envl} \sim 0.72$, due to a very weak sensitivy of the g-mode pulsation frequencies to this parameter.

The inner core structure is also unraveled, pointing to a rather large mixed core with a fractional mass $\log q({\rm core}) = -0.295 \pm 0.018$, corresponding to $M_{\rm core} = 0.198 \pm 0.015\ M_\odot$. This size is reached while the estimated remaining helium mass fraction in that region is $X({\rm He})_{\rm core} = 0.57^{+0.08}_{-0.03}$. TIC 278659026 is therefore close to the mid-stage of its helium-burning phase, as it has transformed about 43% of its helium into carbon and oxygen. We point out that the value obtained for the core size is comparable to some estimates already provided for this quantity by Charpinet et al. (2011) for the star KIC 02697388 (solution 2) and by Van Grootel et al. (2010b) for the star KPD 0629-0016. The latter in particular, although more massive as it has a canonical mass of $0.471 \pm 0.002\ M_\odot$, happens to be nearly at the same stage of its core helium-burning phase, with $\sim 59\%$ (in mass) of helium left in the central region, while its estimated core size is $\log q({\rm core}) = -0.27 \pm 0.01$ ($M_{\rm core} = 0.22 \pm 0.01\ M_\odot$).

Nonetheless, Van Grootel et al. (2010a) also provides a seismic estimate of the core mass for the sdB pulsator KPD 1943+4058, but obtains a significantly larger measurement for this quantity. This star may need to be re-investigated with our most recent modelling tools applied to the full data set now available (Van Grootel et al. 2010a analysis was based on *Kepler*'s Q0 light curve only). Remarkably, and for the first time in a hot B subdwarf star, our present seismic modelling of TIC 278659026 also provides an estimate for the oxygen mass fraction in the helium burning core. We find that $X(\mathrm{O})_{\mathrm{core}} = 0.16^{+0.13}_{-0.07}$ and consequently the estimated carbon mass fraction is $X(\mathrm{C})_{\mathrm{core}} = 0.27^{+0.08}_{-0.15}$. These values, along with knowing the size of the core, are of high interest as they are directly connected with the uncertain rate of the $^{12}\mathrm{C}(\alpha,\gamma)^{16}\mathrm{O}$ nuclear reaction, which is fundamental in many areas of astrophysics.

3.4.3. Frequency match and mode identification

The optimal seismic model uncovered for TIC 278659026 provides the closest match to the observed frequencies obtained thus far for a g-mode pulsating sdB star. With an average relative dispersion $|\overline{\Delta X/X}| = 0.07\%$ ($X = P$ or ν), which corresponds, on an absolute scale, to $|\overline{\Delta P}| = 3.16$ second and $|\overline{\Delta\nu}| = 0.161$ μHz for 20 frequencies matched simultaneously, this fit outperforms previous comparable studies presented by Van Grootel et al. (2010a,b) and Charpinet et al. (2011) by a factor $\sim 3-5$ on the achieved relative dispersion. This significant gain in matching precision is clearly due to the improvements implemented in stellar models used in the present analysis relative to these older studies (see Section 3.1). We point out that this ability to better reproduce the observed oscillation spectrum is certainly the main factor that has allowed us to extract more information about the internal structure of TIC 278659026. We also find that our best fit reaches an absolute precision in frequency that is ~ 2.5 times better than the formal resolution of this *TESS* observing run (which, we recall, is 0.415 μHz). However, since the actual precision on each frequency measurement is of the order of one-tenth of the formal resolution (see again Table 1), the match is not perfect and significant room still remains to further improve our seismic modelling. A better description of the helium-burning core boundary to produce profiles that comply more accurately to those produced by, e.g., semi-convection is among future improvements that we plan to introduce.

All the details about the g-mode spectrum of the optimal model, the frequency fit, and the associated mode identification are given in Table 3 and illustrated in Fig. 13. The table provides, for each mode, the degree ℓ and radial order k, the computed adiabatic frequency and period (ν_{th} and P_{th}), their corresponding matched frequency and period (ν_{obs} and P_{obs}) when available, the logarithm of the kinetic energy (or inertia) of the mode ($\log E_{\mathrm{kin}}$; see, e.g., Charpinet et al. 2000), the first-order Ledoux coefficient for slow rigid rotation ($C_{k\ell}$), and the relative and absolute differences between the observed and computed values $\Delta X/X$, ΔP, and $\Delta\nu$, when available. We find that the 20 independent frequencies of TIC 278659026 are well interpreted as 13 $\ell = 1$ and 7 $\ell = 2$ g-modes of low-to-intermediate radial orders ranging from $k = 7-57$. The observed spectrum is clearly incomplete, with many undetected eigenfrequencies that are present in the model. Many of these unseen frequencies may just be excited by the driving engine, but to amplitude levels that are simply below the detection threshold reached with the available data. The mechanisms controling mode amplitude saturation are not well known. Moreover, amplitudes can change over long timescales in g-mode sdB pulsators, likely due to nonlinear mode interactions, as documented by Zong et al. (2016a, 2018). In this context, bottom panel of Fig. 13 suggests that modes of lowest inertia (or kinetic energy), which are susceptible to be excited to higher intrinsic amplitudes for a given amount of energy, seem indeed to be the ones most seen in the spectrum of TIC 278659026. Hence, the overall amplitude distribution (and detectability) of g-modes in sdB pulsators likely has mode inertia as one of its controling factors, but other effects play an important role too.

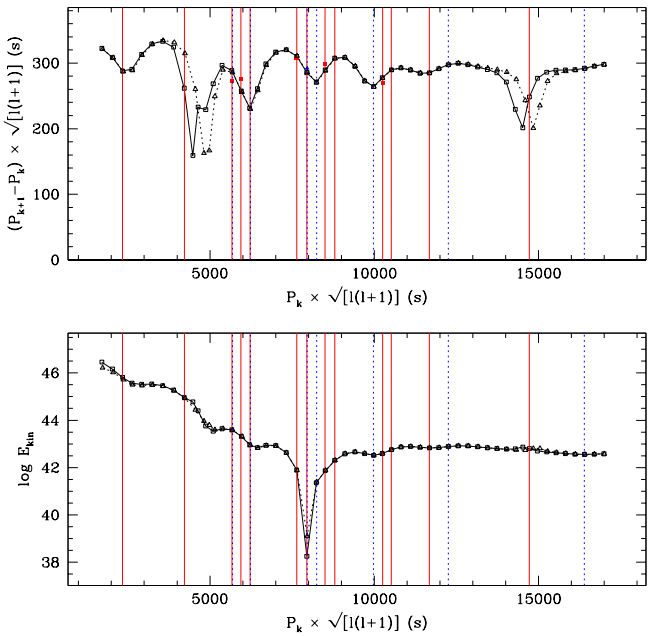

Fig. 13. *Top panel*: Period spectrum corresponding to the optimal seismic model uncovered for TIC 278659026 and represented in terms of the reduced period spacing, $(P_{k+1} - P_k).\sqrt{\ell(\ell+1)}$ (in seconds) as a function of reduced period, $P_k.\sqrt{\ell(\ell+1)}$ (in seconds). Open squares connected by plain segments is the $\ell = 1$ series of modes and open triangles connected by dotted segments are $\ell = 2$ modes. The range of radial orders covered spans from $k = 5$ to $k = 60$, as in Table 3. Plain and dotted vertical lines indicate the reduced periods of the observed modes matched to $\ell = 1$ and $\ell = 2$ modes, respectively. When two observed modes of same degree have consecutive radial orders, an observed reduced period spacing is also indicated (filled squares and filled triangles for $\ell = 1$ and $\ell = 2$ modes, respectively). *Bottom panel*: same as above, but for the logarithm of the kinetic energy (or inertia), $\log E_{\mathrm{kin}}$, of the modes as a function of reduced period.

Despite the relatively sparse distribution, several observed frequencies are grouped into 2 or 3 modes of consecutive radial order. Top panel of Fig. 13 illustrates the pulsation spectrum of the best-fit model and the matched observed modes in terms of their reduced period spacing, $\Delta P_k = (P_{k+1} - P_k).\sqrt{\ell(\ell+1)}$, plotted as a function of reduced period, $P_k.\sqrt{\ell(\ell+1)}$, for the dipole and quadrupole series. This representation highlights a series of oscillations and dips that occur around the theoretical average reduced

period spacing, Π_0, whose value is 278.4 s for the optimal model[9], which are typical of trapping effects generated by rapid changes of the chemical composition, e.g., at the core edge or at the mantle/envelope transition (see Charpinet et al. 2014a, and references therein). As expected from asymptotic relations (Charpinet et al. 2000, 2002), all modes of same radial order but different degree ℓ almost always overlap in the reduced period space and follow the same patterns. We note a slight distorsion to this rule around two dips where the trapping occurs with a shift of $\Delta k = 1$ for $\ell = 2$ modes compared to their $\ell = 1$ counterpart. This distortion appears related to the sharp transition at the core boundary which has the particularity to be located close to the inner turning point of the gravity waves in their resonant cavity. Overall, we find that the observed periods and their identification match quite well the model spectrum properties. However, small discrepancies are still noticeable reflecting, as mentioned previously, the greatly improved but still imperfect models used in this asteroseismic analysis.

4. Summary and conclusion

We have reported on the discovery of a new bright g-mode pulsating hot B subdwarf star, TIC 278659026 (EC 21494-7078), by the NASA/ *TESS* mission. This object is just one of the hundreds of evolved compact stars (mostly hot subdwarfs and white dwarfs) monitored with the 120s-cadence mode in the first *TESS* sector. This effort is part of a larger program driven by TASC Working Group 8 to survey thousands of bright evolved compact stars for variability. The data consists of 27.88 days of photometry with a nearly continuous coverage, thus offering an exquisite view on the pulsation spectrum of TIC 278659026. The analysis of the time series revealed the presence of many frequencies in the 90–650 μHz range, among which 20 are interpreted as independent low-degree ($\ell = 1$ and 2) gravity modes later used to provide strong seismic constraints on the structure and fundamental parameters of the star.

The asteroseismic investigation of TIC 278659026 was conducted with our state-of-the-art modelling and optimization tools. These implement a forward modelling approach developed over the past 15 years and described in some detail in, e.g., Van Grootel et al. (2013), Giammichele et al. (2016), and references therein. Compared to former analyses of g-mode sdB pulsators, we used an improved version of the Montréal third-generation (3G) stellar models (Van Grootel et al. 2010a,b; Charpinet et al. 2011) implementing a more complex envelope structure that allows for double-layered hydrogen/helium profiles. Such profiles are characteristic of the outcome of gravitational settling for the coolest hot subdwarfs, when helium lacks time to completely sink below their relatively thick envelopes during the lifetime of the star on the Extreme Horizontal Branch. Former 3G models were indeed assuming pure hydrogen envelopes, not fully appropriate to analyse the coolest g-mode sdB pulsators.

The extensive search for a best-fit seismic model reproducing the 20 frequencies that characterize TIC 278659026 led to the identification of a well-defined solution in close agreement with available constraints on $T_{\rm eff}$ and $\log g$ derived from spectroscopy (Németh et al. 2012). The solution also agrees remarkably well with the distance measured independently from the *Gaia* trigonometric parallax, through a comparison with the "seismic distance" estimated from the model properties (see Section 3.3.1 and Table 2), and with the mass estimated from combining the fit of the spectral energy distribution and the *Gaia* parallax. All constitute important tests validating the accuracy of the identified seismic model. Through this solution, asteroseismology is giving us extensive information on fundamental parameters and internal structure in TIC 278659026. In particular, we find that this star has a mass of $0.391 \pm 0.013\ M_\odot$, which is significantly lower than the canonical mass of $0.47\ M_\odot$ characterizing most hot B subdwarfs. According to Han et al. (2002, 2003), such a low-mass sdB star is most likely produced by the first stable Roche lobe overflow (RLOF) channel, although there is presently no indication of the presence of a stellar companion. The low mass inferred suggest that TIC 278659026 must have started helium burning in non-degenerate conditions, i.e., before reaching the critical mass that triggers the helium flash. Stellar evolution calculations show that main sequence stars with masses above $\sim 2\ M_\odot$ ignite helium before electron degeneracy occurs, and consequently have less massive cores. TIC 278659026 could, in this context, become the first evidence of a rare hot B subdwarf star that originates from a massive ($\gtrsim 2\ M_\odot$) red giant, an alternative formation channel investigated by Hu et al. (2008). We last note that the inferred mass and the presence of pulsations at such high effective temperature rule out the suggestion from Kawka et al. (2015) that TIC 278659026 may be an ELM white-dwarf progenitor.

Other notable results include constraints on the chemical stratification inside the star. We found, in particular, that TIC 278659026 has a rather thick H-rich envelope, with $M(H) = 0.0037 \pm 0.0017\ M_\odot$ (computed from $\log q(\mathrm{envl}) = -2.11 \pm 0.19$; see Table 2), whose structure includes a double-layered He/H distribution caused by still ongoing gravitational settling of helium. The core, for its part, is found to be more extended than typically predicted by standard evolution models, reaching a mass of $0.198 \pm 0.015\ M_\odot$ ($\log q(\mathrm{core}) = -0.295 \pm 0.018$) while TIC 278659026 is at about half-way of its evolution through the core helium-burning phase. The mass fraction of helium remaining at the center of the star is estimated to be $X(\mathrm{He})_{\rm core} = 0.57^{+0.08}_{-0.03}$. Therefore, this star constitutes another case that suggests, along with three other hot subdwarfs analyzed previously and recent evidence from white dwarf asteroseismology, that helium-burning cores are larger than predicted by current implementations of physical processes shaping the core structure in stellar evolution calculations. The present measurement thus provides a very useful quantitative constraint to explore this issue. We also found that the oxygen mass fraction produced in the core (and consequently the amount of carbon present) is constrained for the first time in a sdB star (and by extension in a core helium burning star) to a quite interesting level of precision, $X(\mathrm{O})_{\rm core} = 0.16^{+0.13}_{-0.07}$ (and for carbon, $X(\mathrm{C})_{\rm core} = 0.27^{+0.08}_{-0.15}$). These values, along with the determination of the core size mentioned previously, are directly connected to the $^{12}\mathrm{C}(\alpha,\gamma)^{16}\mathrm{O}$ nuclear reaction, which is important in many areas of astrophysics but whose rate is still highly uncertain. TIC 278659026, through the present

[9] In the asymptotic limit, $\Pi_0 = 2\pi^2 \left(\int_0^R \frac{|N|}{r} dr \right)^{-1}$

seismic analysis, may thus become an important test to improve our knowledge on this issue as well.

We conclude this paper by emphasizing that this particularly insightful analysis of the hot B subdwarf star TIC 278659026 discovered to be pulsating by *TESS,* and based on only one sector, is a demonstration that this instrument, even if not technically optimized for asteroseismology of hot and faint evolved compact stars, is providing outstanding data that can significantly drive this field forward. *TESS* greatest advantage over previous similar projects (*K2*, *Kepler*, *CoRoT*, and *MOST*) is that it will survey many more hot subdwarf stars during the two years of its main mission. Among them, many will be pulsating sdB stars with a comparable seismic potential and it will allow us to probe the interior and core structure of these stars over wider ranges of masses and ages on the extreme horizontal branch. *TESS* contribution to this research area should therefore prove very significant.

Acknowledgements. Stéphane Charpinet acknowledges financial support from the Centre National d'Études Spatiales (CNES, France) and from the Agence Nationale de la Recherche (ANR, France) under grant ANR-17-CE31-0018, funding the INSIDE project. This work was granted access to the high-performance computing resources of the CALMIP computing centre under allocation number 2018-p0205. G.F. acknowledges the contribution of the Canada Research Chair Program. W.Z. aknowledges the support from the National Natural Science Foundation of China (NSFC) through the grant 11833002, the support from the China Postdoctoral Science Foundation through the grant 2018M641244 and the LAMOST fellowship as a Youth Researcher which is supported by the Special Funding for Advanced Users, budgeted and administrated by the Center for Astronomical Mega-Science, Chinese Academy of Sciences (CAMS). V.V.G. is an F.R.S.-FNRS Research Associate. ZsB and ÁS acknowledge the financial support of the GINOP-2.3.2-15-2016-00003, K-115709, K-113117, K-119517 and PD-123910 grants of the Hungarian National Research, Development and Innovation Office (NKFIH), and the Lendület Program of the Hungarian Academy of Sciences, project No. LP2018-7/2018. DK acknowledges financial support form the University of the Western Cape. I. P. acknowledges funding by the Deutsche Forschungsgemeinschaft under grant GE2506/12-1. AP and PK-S acknowledge support from the NCN grant no. 2016/21/B/ST9/01126. We thank Andreas Irrgang and Simon Kreuzer for developing the SED fitting tool. The authors acknowledge the *TESS* and TASC teams and everyone who has contributed to making this mission possible. Funding for the *TESS* mission is provided by NASA's Science Mission Directorate. This work has made use of data from the European Space Agency (ESA) mission *Gaia* (`https://www.cosmos.esa.int/gaia`), processed by the *Gaia* Data Processing and Analysis Consortium (DPAC, `https://www.cosmos.esa.int/web/gaia/dpac/consortium`). Funding for the DPAC has been provided by national institutions, in particular the institutions participating in the *Gaia* Multilateral Agreement. The national facility capability for SkyMapper has been funded through ARC LIEF grant LE130100104 from the Australian Research Council, awarded to the University of Sydney, the Australian National University, Swinburne University of Technology, the University of Queensland, the University of Western Australia, the University of Melbourne, Curtin University of Technology, Monash University and the Australian Astronomical Observatory. SkyMapper is owned and operated by The Australian National University's Research School of Astronomy and Astrophysics. The survey data were processed and provided by the SkyMapper Team at ANU. The SkyMapper node of the All-Sky Virtual Observatory (ASVO) is hosted at the National Computational Infrastructure (NCI). Development and support the SkyMapper node of the ASVO has been funded in part by Astronomy Australia Limited (AAL) and the Australian Government through the Commonwealth's Education Investment Fund (EIF) and National Collaborative Research Infrastructure Strategy (NCRIS), particularly the National eResearch Collaboration Tools and Resources (NeCTAR) and the Australian National Data Service Projects (ANDS). This publication makes use of data products from the Wide-field Infrared Survey Explorer, which is a joint project of the University of California, Los Angeles, and the Jet Propulsion Laboratory/California Institute of Technology, funded by the National Aeronautics and Space Administration. This publication makes use of data products from the Two Micron All Sky Survey, which is a joint project of the University of Massachusetts and the Infrared Processing and Analysis Center/California Institute of Technology, funded by the National Aeronautics and Space Administration and the National Science Foundation.

References

Baglin, A., Auvergne, M., Boisnard, L., et al. 2006, in COSPAR, Plenary Meeting, Vol. 36, 36th COSPAR Scientific Assembly, 3749–+
Baran, A., Oreiro, R., Pigulski, A., et al. 2009, MNRAS, 392, 1092
Baran, A. S., Reed, M. D., Østensen, R. H., Telting, J. H., & Jeffery, C. S. 2017, A&A, 597, A95
Borucki, W. J., Koch, D., Basri, G., et al. 2010, Science, 327, 977
Brassard, P. & Charpinet, S. 2008, Ap&SS, 316, 107
Brassard, P. & Fontaine, G. 2008, in ASPCS, Vol. 392, Hot Subdwarf Stars and Related Objects, ed. U. Heber, C. S. Jeffery, & R. Napiwotzki, 261
Brassard, P. & Fontaine, G. 2009, Journal of Physics Conference Series, 172, 012016
Brassard, P., Fontaine, G., Billères, M., et al. 2001, ApJ, 563, 1013
Brassard, P., Pelletier, C., Fontaine, G., & Wesemael, F. 1992, ApJS, 80, 725
Charpinet, S., Brassard, P., Fontaine, G., et al. 2009, in American Institute of Physics Conference Series, Vol. 1170, American Institute of Physics Conference Series, ed. J. A. Guzik & P. A. Bradley, 585–596
Charpinet, S., Brassard, P., Van Grootel, V., & Fontaine, G. 2014a, in Astronomical Society of the Pacific Conference Series, Vol. 481, 6th Meeting on Hot Subdwarf Stars and Related Objects, ed. V. van Grootel, E. Green, G. Fontaine, & S. Charpinet, 179
Charpinet, S., Fontaine, G., & Brassard, P. 2001, PASP, 113, 775
Charpinet, S., Fontaine, G., Brassard, P., et al. 1997, ApJ, 483, L123
Charpinet, S., Fontaine, G., Brassard, P., & Dorman, B. 1996, ApJ, 471, L103
Charpinet, S., Fontaine, G., Brassard, P., & Dorman, B. 2000, ApJS, 131, 223
Charpinet, S., Fontaine, G., Brassard, P., & Dorman, B. 2002, ApJS, 139, 487
Charpinet, S., Fontaine, G., Brassard, P., Green, E. M., & Chayer, P. 2005, A&A, 437, 575
Charpinet, S., Giammichele, N., Brassard, P., Van Grootel, V., & Fontaine, G. 2015, in Astronomical Society of the Pacific Conference Series, Vol. 493, 19th European Workshop on White Dwarfs, ed. P. Dufour, P. Bergeron, & G. Fontaine, 151
Charpinet, S., Giammichele, N., Zong, W., et al. 2018, Open Astronomy, 27, 112
Charpinet, S., Green, E. M., Baglin, A., et al. 2010, A&A, 516, L6
Charpinet, S., Van Grootel, V., Brassard, P., & Fontaine, G. 2014b, in IAU Symposium, Vol. 301, Precision Asteroseismology, ed. J. A. Guzik, W. J. Chaplin, G. Handler, & A. Pigulski, 397–398
Charpinet, S., Van Grootel, V., Brassard, P., et al. 2014c, in Astronomical Society of the Pacific Conference Series, Vol. 481, 6th Meeting on Hot Subdwarf Stars and Related Objects, ed. V. van Grootel, E. Green, G. Fontaine, & S. Charpinet, 105
Charpinet, S., Van Grootel, V., Fontaine, G., et al. 2011, A&A, 530, A3
Charpinet, S., Van Grootel, V., Reese, D., et al. 2008, A&A, 489, 377
Copperwheat, C. M., Morales-Rueda, L., Marsh, T. R., Maxted, P. F. L., & Heber, U. 2011, MNRAS, 415, 1381
Cutri, R. M. & et al. 2013, VizieR Online Data Catalog, 2328
Deeming, T. J. 1976, Ap&SS, 42, 257
Dorman, B., Rood, R. T., & O'Connell, R. W. 1993, ApJ, 419, 596
Fontaine, G., Brassard, P., Charpinet, S., et al. 2003, ApJ, 597, 518
Fontaine, G., Brassard, P., Charpinet, S., et al. 2012, A&A, 539, A12
Gaia Collaboration, Brown, A. G. A., Vallenari, A., et al. 2018, A&A, 616, A1
Gaia Collaboration, Prusti, T., de Bruijne, J. H. J., et al. 2016, A&A, 595, A1
Geier, S. & Heber, U. 2012, A&A, 543, A149
Geier, S., Heber, U., Podsiadlowski, P., et al. 2010, A&A, 519, A25
Ghasemi, H., Moravveji, E., Aerts, C., Safari, H., & Vučković, M. 2017, MNRAS, 465, 1518
Giammichele, N., Charpinet, S., Brassard, P., & Fontaine, G. 2017, A&A, 598, A109
Giammichele, N., Charpinet, S., Fontaine, G., et al. 2018, Nature, 554, 73

Giammichele, N., Fontaine, G., Brassard, P., & Charpinet, S. 2016, ApJS, 223, 10
Gilliland, R. L., Brown, T. M., Christensen-Dalsgaard, J., et al. 2010, PASP, 122, 131
Green, E. M., Fontaine, G., Reed, M. D., et al. 2003, ApJ, 583, L31
Han, Z., Podsiadlowski, P., Maxted, P. F. L., & Marsh, T. R. 2003, MNRAS, 341, 669
Han, Z., Podsiadlowski, P., Maxted, P. F. L., Marsh, T. R., & Ivanova, N. 2002, MNRAS, 336, 449
Heber, U. 2016, PASP, 128, 082001
Heber, U., Irrgang, A., & Schaffenroth, J. 2018, Open Astronomy, 27, 35
Henden, A. A., Templeton, M., Terrell, D., et al. 2016, VizieR Online Data Catalog, 2336
Høg, E., Fabricius, C., Makarov, V. V., et al. 2000, A&A, 355, L27
Howell, S. B., Sobeck, C., Haas, M., et al. 2014, PASP, 126, 398
Hu, H., Dupret, M.-A., Aerts, C., et al. 2008, A&A, 490, 243
Hu, H., Glebbeek, E., Thoul, A. A., et al. 2010, A&A, 511, A87
Hu, H., Nelemans, G., Aerts, C., & Dupret, M.-A. 2009, A&A, 508, 869
Jeffery, C. S. & Saio, H. 2006, MNRAS, 371, 659
Jiménez-Esteban, F. M., Caballero, J. A., & Solano, E. 2011, A&A, 525, A29
Kawka, A., Vennes, S., O'Toole, S., et al. 2015, MNRAS, 450, 3514
Kern, J. W., Reed, M. D., Baran, A. S., Østensen, R. H., & Telting, J. H. 2017, MNRAS, 465, 1057
Ketzer, L., Reed, M. D., Baran, A. S., et al. 2017, MNRAS, 467, 461
Kilkenny, D., Fontaine, G., Green, E. M., & Schuh, S. 2010, Information Bulletin on Variable Stars, 5927, 1
Kilkenny, D., Koen, C., O'Donoghue, D., & Stobie, R. S. 1997, MNRAS, 285, 640
Németh, P., Kawka, A., & Vennes, S. 2012, MNRAS, 427, 2180
O'Donoghue, D., Kilkenny, D., Koen, C., et al. 2013, MNRAS, 431, 240
Østensen, R. H., Silvotti, R., Charpinet, S., et al. 2011, MNRAS, 414, 2860
Østensen, R. H., Silvotti, R., Charpinet, S., et al. 2010, MNRAS, 409, 1470
Østensen, R. H., Telting, J. H., Reed, M. D., et al. 2014, A&A, 569, A15
Randall, S. K., Fontaine, G., Green, E. M., et al. 2006a, ApJ, 643, 1198
Randall, S. K., Green, E. M., Fontaine, G., et al. 2006b, ApJ, 645, 1464
Randall, S. K., Van Grootel, V., Fontaine, G., Charpinet, S., & Brassard, P. 2009, A&A, 507, 911
Reed, M. D., Baran, A., Quint, A. C., et al. 2011, MNRAS, 414, 2885
Reed, M. D., Foster, H., Telting, J. H., et al. 2014, MNRAS, 440, 3809
Reed, M. D., Telting, J. H., Ketzer, L., et al. 2019, MNRAS, 483, 2282
Ricker, G. R., Winn, J. N., Vanderspek, R., et al. 2014, in Proc. SPIE, Vol. 9143, Space Telescopes and Instrumentation 2014: Optical, Infrared, and Millimeter Wave, 914320
Saffer, R. A., Bergeron, P., Koester, D., & Liebert, J. 1994, ApJ, 432, 351
Schuh, S., Huber, J., Dreizler, S., et al. 2006, A&A, 445, L31
Skrutskie, M. F., Cutri, R. M., Stiening, R., et al. 2006, AJ, 131, 1163
Telting, J. H., Baran, A. S., Nemeth, P., et al. 2014, A&A, 570, A129
Van Grootel, V., Charpinet, S., Brassard, P., Fontaine, G., & Green, E. M. 2013, A&A, 553, A97
Van Grootel, V., Charpinet, S., Fontaine, G., & Brassard, P. 2008a, A&A, 483, 875
Van Grootel, V., Charpinet, S., Fontaine, G., et al. 2008b, A&A, 488, 685
Van Grootel, V., Charpinet, S., Fontaine, G., et al. 2010a, ApJ, 718, L97
Van Grootel, V., Charpinet, S., Fontaine, G., Green, E. M., & Brassard, P. 2010b, A&A, 524, A63
Walker, G., Matthews, J., Kuschnig, R., et al. 2003, PASP, 115, 1023
Wolf, C., Onken, C. A., Luvaul, L. C., et al. 2018, PASA, 35, e010
Zong, W., Charpinet, S., Fu, J.-N., et al. 2018, ApJ, 853, 98
Zong, W., Charpinet, S., & Vauclair, G. 2016a, A&A, 594, A46
Zong, W., Charpinet, S., Vauclair, G., Giammichele, N., & Van Grootel, V. 2016b, A&A, 585, A22

[1] Institut de Recherche en Astrophysique et Planétologie, CNRS, Université de Toulouse, CNES, 14 avenue Edouard Belin, F-31400 Toulouse, France
e-mail: stephane.charpinet@irap.omp.eu
[2] Département de Physique, Université de Montréal, Québec H3C 3J7, Canada
[3] Space sciences, Technologies and Astrophysics Research (STAR) Institute, Université de Liège, 19C Allée du six-août, B-4000 Liège, Belgium
[4] Department of Astronomy, Beijing Normal University, Beijing 100875, China
[5] Dr. Karl Remeis-Observatory & ECAP, Astronomical Institute, Friedrich-Alexander University Erlangen-Nürnberg (FAU), Sternwartstr. 7, 96049, Bamberg, Germany
[6] Konkoly Observatory, MTA Research Centre for Astronomy and Earth Sciences, Konkoly Thege Miklós út 15-17, H-1121 Budapest
[7] MTA CSFK Lendület Near-Field Cosmology Research Group
[8] Institute for Physics and Astronomy, University of Potsdam, Karl-Liebknecht-Str. 24/25, D-14476 Potsdam, Germany
[9] Steward Observatory, University of Arizona, 933 North Cherry Avenue, Tucson, AZ, 85721, USA
[10] Department of Astronomy, Boston University, 725 Commonwealth Ave., Boston, MA 02215 - USA
[11] Department of Physics and Astronomy, University of the Western Cape, Private Bag X17, Bellville 7535, South Africa
[12] Department of Physics, Astronomy, and Materials Science, Missouri State University, Springfield, MO 65897, USA
[13] INAF-Osservatorio Astrofisico di Torino, strada dell'Osservatorio 20, I-10025 Pino Torinese, Italy
[14] Nordic Optical Telescope, Rambla José Ana Fernández Pérez 7, 38711 Breña Baja, Spain
[15] Instituto de Física y Astronomía, Universidad de Valparaiso, Gran Bretaña 1111, Playa Ancha, Valparaíso 2360102, Chile
[16] South African Astronomical Observatory, PO Box 9, Observatory, Cape Town 7935, South Africa
[17] Uniwersytet Pedagogiczny, Obserwatorium na Suhorze, ul. Podchorżych 2, 30-084 Kraków, Polska
[18] Max-Planck-Institut für Sonnensystemforschung (MPS), Justus-von-Liebig-Weg 3, D-37077 Göttingen, Germany; Department of Physics and Astronomy, Stellar Astrophysics Centre, Aarhus University, Ny Munkegade 120, 8000 Aarhus C, Denmark
[19] XCP-6, MS F699, Los Alamos National Laboratory, Los Alamos, NM 87545 USA
[20] Space Telescope Science Institute, 3700 San Martin Drive, Baltimore, MD 21218, USA
[21] Department of Physics and Astronomy, Iowa State University, Ames, IA 50011, USA
[22] Instytut Astronomiczny, Uniwersytet Wrocławski, ul. Kopernika 11, 51-622 Wrocław, Poland
[23] Sydney Institute for Astronomy (SIfA), School of Physics, The University of Sydney, NSW 2006, Australia

Table 4. Mode identification and details of the optimal frequency match obtained for TIC 278659026. The mean relative dispersion of the fit is $\overline{\Delta X/X} = 0.07\%$ ($X = P$ or ν), corresponding to $\overline{\Delta P} = 3.16$ s, $\overline{\Delta\nu} = 0.161$ μHz, and $S^2 = 0.139$.

l	k	$\nu_{\rm obs}$ (μHz)	$\nu_{\rm th}$ (μHz)	$P_{\rm obs}$ (s)	$P_{\rm th}$ (s)	$\log E$ (erg)	C_{kl}	$\Delta X/X$ (%)	ΔP (s)	$\Delta\nu$ (μHz)	Amplitude (%)	Id.
1	5	...	827.455	...	1208.52	46.456	0.4849	...	...	...	...	
1	6	...	696.183	...	1436.40	46.165	0.4846	...	...	...	...	
1	7	604.580	604.358	1654.04	1654.65	45.812	0.4849	−0.04	−0.61	+0.221	0.0212	f_{19}
1	8	...	538.122	...	1858.32	45.570	0.4859	...	...	...	...	
1	9	...	484.536	...	2063.83	45.519	0.4881	...	...	...	...	
1	10	...	437.573	...	2285.33	45.530	0.4899	...	...	...	...	
1	11	...	397.132	...	2518.06	45.463	0.4910	...	...	...	...	
1	12	...	363.148	...	2753.70	45.273	0.4913	...	...	...	...	
1	13	335.033	335.244	2984.78	2982.91	44.964	0.4891	+0.06	+1.88	−0.211	0.0735	f_4
1	14	...	315.659	...	3167.98	44.776	0.4707	...	...	...	...	
1	15	...	304.833	...	3280.48	44.407	0.4733	...	...	...	...	
1	16	...	290.261	...	3445.18	43.753	0.4846	...	...	...	...	
1	17	...	277.235	...	3607.05	43.545	0.4880	...	...	...	...	
1	18	...	263.368	...	3796.96	43.643	0.4934	...	...	...	...	
1	19	249.269	249.584	4011.74	4006.66	43.594	0.4946	+0.13	+5.07	−0.315	0.3184	f_1
1	20	237.829	237.490	4204.70	4210.70	43.322	0.4944	−0.14	−6.00	+0.339	0.0200	f_{21}
1	21	227.285	227.646	4399.77	4392.79	42.960	0.4930	+0.16	+6.98	−0.361	0.0810	f_3
1	22	...	219.469	...	4556.46	42.841	0.4935	...	...	...	...	
1	23	...	210.919	...	4741.16	42.947	0.4957	...	...	...	...	
1	24	...	201.920	...	4952.46	42.933	0.4968	...	...	...	...	
1	25	...	193.185	...	5176.39	42.635	0.4971	...	...	...	...	
1	26	185.014	185.086	5404.99	5402.89	41.899	0.4970	+0.04	+2.10	−0.072	0.0452	f_7
1	27	177.869	177.864	5622.13	5622.27	38.251	0.4964	−0.00	−0.14	+0.005	0.0223	f_{16}
1	28	...	171.701	...	5824.09	41.361	0.4955	...	...	...	...	
1	29	166.256	166.232	6014.82	6015.70	41.870	0.4959	−0.01	−0.87	+0.024	0.0266	f_{12}
1	30	160.622	160.757	6225.81	6220.57	42.306	0.4969	+0.08	+5.24	−0.135	0.0655	f_6
1	31	...	155.327	...	6438.01	42.584	0.4975	...	...	...	...	
1	32	...	150.236	...	6656.19	42.661	0.4975	...	...	...	...	
1	33	...	145.671	...	6864.76	42.592	0.4971	...	...	...	...	
1	34	...	141.693	...	7057.50	42.521	0.4966	...	...	...	...	
1	35	137.912	138.039	7251.01	7244.32	42.595	0.4970	+0.09	+6.69	−0.127	0.0192	f_{23}
1	36	134.387	134.398	7441.22	7440.61	42.756	0.4976	+0.01	+0.61	−0.011	0.0375	f_{10}
1	37	...	130.797	...	7645.43	42.869	0.4980	...	...	...	...	
1	38	...	127.350	...	7852.39	42.893	0.4980	...	...	...	...	
1	39	...	124.116	...	8057.00	42.858	0.4980	...	...	...	...	
1	40	121.144	121.092	8254.62	8258.21	42.828	0.4979	−0.04	−3.59	+0.053	0.0194	f_{22}
1	41	...	118.207	...	8459.72	42.846	0.4980	...	...	...	...	
1	42	...	115.396	...	8665.81	42.891	0.4982	...	...	...	...	
1	43	...	112.660	...	8876.27	42.921	0.4983	...	...	...	...	
1	44	...	110.034	...	9088.07	42.914	0.4984	...	...	...	...	
1	45	...	107.544	...	9298.48	42.880	0.4984	...	...	...	...	
1	46	...	105.193	...	9506.34	42.838	0.4983	...	...	...	...	
1	47	...	102.970	...	9711.59	42.804	0.4982	...	...	...	...	
1	48	...	100.876	...	9913.21	42.782	0.4979	...	...	...	...	
1	49	...	98.962	...	10104.90	42.791	0.4969	...	...	...	...	
1	50	...	97.399	...	10267.04	42.872	0.4945	...	...	...	...	
1	51	96.073	96.065	10408.72	10409.58	42.806	0.4955	−0.01	−0.86	+0.008	0.0324	f_{11}
1	52	...	94.473	...	10585.06	42.701	0.4976	...	...	...	...	
1	53	...	92.757	...	10780.91	42.658	0.4983	...	...	...	...	
1	54	...	91.047	...	10983.32	42.628	0.4986	...	...	...	...	
1	55	...	89.383	...	11187.83	42.596	0.4987	...	...	...	...	
1	56	...	87.776	...	11392.59	42.570	0.4987	...	...	...	...	
1	57	...	86.225	...	11597.63	42.560	0.4988	...	...	...	...	
1	58	...	84.716	...	11804.14	42.568	0.4989	...	...	...	...	
1	59	...	83.243	...	12013.04	42.582	0.4990	...	...	...	...	
1	60	...	81.808	...	12223.77	42.584	0.4991	...	...	...	...	
2	5	...	1413.333	...	707.55	46.223	0.1524	...	...	...	...	
2	6	...	1192.361	...	838.67	46.024	0.1517	...	...	...	...	
2	7	...	1036.894	...	964.42	45.718	0.1517	...	...	...	...	
2	8	...	924.614	...	1081.53	45.496	0.1526	...	...	...	...	

Table 4. continued.

l	k	$\nu_{\rm obs}$ (μHz)	$\nu_{\rm th}$ (μHz)	$P_{\rm obs}$ (s)	$P_{\rm th}$ (s)	$\log E$ (erg)	C_{kl}	$\Delta X/X$ (%)	ΔP (s)	$\Delta\nu$ (μHz)	Amplitude (%)	Id.
2	9	...	833.753	...	1199.40	45.463	0.1548	...	...	...	...	
2	10	...	753.739	...	1326.72	45.492	0.1568	...	...	...	...	
2	11	...	684.500	...	1460.92	45.439	0.1581	...	...	...	...	
2	12	...	625.989	...	1597.47	45.255	0.1587	...	...	...	...	
2	13	...	577.092	...	1732.83	44.925	0.1587	...	...	...	...	
2	14	...	537.254	...	1861.32	44.446	0.1568	...	...	...	...	
2	15	...	508.264	...	1967.48	43.968	0.1497	...	...	...	...	
2	16	...	491.646	...	2033.98	43.796	0.1426	...	...	...	...	
2	17	...	475.730	...	2102.03	43.597	0.1508	...	...	...	...	
2	18	...	453.771	...	2203.75	43.645	0.1583	...	...	...	...	
2	19	430.875	430.663	2320.86	2322.00	43.589	0.1607	−0.05	−1.14	+0.212	0.0686	f_5
2	20	...	410.071	...	2438.60	43.320	0.1609	...	...	...	...	
2	21	393.032	393.215	2544.32	2543.14	42.959	0.1597	+0.05	+1.18	−0.183	0.0251	f_{13}
2	22	...	379.225	...	2636.96	42.831	0.1601	...	...	...	...	
2	23	...	364.632	...	2742.49	42.933	0.1623	...	...	...	...	
2	24	...	349.200	...	2863.69	42.921	0.1634	...	...	...	...	
2	25	...	334.162	...	2992.56	42.625	0.1638	...	...	...	...	
2	26	...	320.185	...	3123.20	41.880	0.1637	...	...	...	...	
2	27	307.720	307.692	3249.70	3250.00	39.115	0.1631	−0.01	−0.30	+0.028	0.0377	f_9
2	28	296.822	297.018	3369.02	3366.80	41.398	0.1622	+0.07	+2.22	−0.196	0.0224	f_{15}
2	29	...	287.589	...	3477.18	41.882	0.1625	...	...	...	...	
2	30	...	278.168	...	3594.95	42.310	0.1636	...	...	...	...	
2	31	...	268.801	...	3720.22	42.589	0.1642	...	...	...	...	
2	32	...	260.000	...	3846.16	42.669	0.1642	...	...	...	...	
2	33	...	252.096	...	3966.74	42.601	0.1638	...	...	...	...	
2	34	245.609	245.207	4071.52	4078.19	42.526	0.1633	−0.16	−6.67	+0.402	0.0240	f_{14}
2	35	...	238.896	...	4185.93	42.594	0.1636	...	...	...	...	
2	36	...	232.611	...	4299.02	42.755	0.1643	...	...	...	...	
2	37	...	226.389	...	4417.17	42.870	0.1647	...	...	...	...	
2	38	...	220.427	...	4536.64	42.895	0.1647	...	...	...	...	
2	39	...	214.831	...	4654.82	42.861	0.1647	...	...	...	...	
2	40	...	209.599	...	4771.03	42.830	0.1646	...	...	...	...	
2	41	...	204.611	...	4887.33	42.846	0.1647	...	...	...	...	
2	42	199.913	199.750	5002.18	5006.25	42.890	0.1649	−0.08	−4.07	+0.163	0.1706	f_2
2	43	...	195.017	...	5127.75	42.920	0.1650	...	...	...	...	
2	44	...	190.472	...	5250.12	42.914	0.1651	...	...	...	...	
2	45	...	186.157	...	5371.82	42.879	0.1651	...	...	...	...	
2	46	...	182.075	...	5492.25	42.836	0.1651	...	...	...	...	
2	47	...	178.202	...	5611.60	42.799	0.1651	...	...	...	...	
2	48	...	174.519	...	5730.05	42.769	0.1651	...	...	...	...	
2	49	...	171.034	...	5846.80	42.745	0.1649	...	...	...	...	
2	50	...	167.810	...	5959.11	42.742	0.1645	...	...	...	...	
2	51	...	165.063	...	6058.31	42.808	0.1632	...	...	...	...	
2	52	...	162.855	...	6140.43	42.809	0.1630	...	...	...	...	
2	53	...	160.348	...	6236.44	42.693	0.1645	...	...	...	...	
2	54	...	157.537	...	6347.71	42.638	0.1651	...	...	...	...	
2	55	...	154.709	...	6463.76	42.600	0.1653	...	...	...	...	
2	56	...	151.951	...	6581.06	42.571	0.1654	...	...	...	...	
2	57	149.432	149.277	6692.01	6698.94	42.560	0.1655	−0.10	−6.93	+0.155	0.0416	f_8
2	58	...	146.674	...	6817.86	42.568	0.1656	...	...	...	...	
2	59	...	144.128	...	6938.26	42.581	0.1657	...	...	...	...	
2	60	...	141.647	...	7059.78	42.583	0.1657	...	...	...	...	